Chapter 6

Linear Stability Analysis

6.1 Overview

Linear stability analysis is used to extend the understanding of the flow dynamics experimentally observed. The analysis is based on the linear disturbance equations. The equations are derived for laminar flow in Section 6.2. The extension to account for turbulence is discussed in Section 6.3. The two solution methods used will be described in Section 6.5. Section 6.4 discusses the interpretation of analysis results and distinguish absolute and convective instability. Section 6.6 compares results using the present analysis methods with results found in literature. Section 6.7 examines the stability characteristics of the flows studied experimentally.

6.2 Laminar disturbance equations

The linear stability equations for near parallel swirling flow were presented informally in Section 1.4.3. A sketch of the derivation of these equations is given here. The starting point are the non-dimensionalized Navier Stokes equations for incompressible flow, neglecting body forces. The continuity equation is given in Equation 6.1. The momentum equations are given in Equation 6.2 in non-dimensional form (Panton, 1984). The radial and axial coordinates for these equation should be considered normalized by a reference dimension.

$$\frac{1}{r}\frac{\partial}{\partial r}(rv_r)+\frac{1}{r}\frac{\partial w}{\partial \theta}+\frac{\partial u}{\partial x}=0 \tag{6.1}$$

$$
\begin{aligned}
\frac{\partial v_r}{\partial t} + v_r\frac{\partial v_r}{\partial r} + \frac{w}{r}\frac{\partial v_r}{\partial \theta} - \frac{w^2}{r} + u\frac{\partial v_r}{\partial x} &= -\frac{\partial p}{\partial r} + \\
&\frac{1}{Re}\left[\frac{\partial}{\partial r}\left(\frac{1}{r}\frac{\partial}{\partial r}(r v_r)\right) + \frac{1}{r^2}\frac{\partial^2 v_r}{\partial \theta^2} - \frac{2}{r^2}\frac{\partial w}{\partial \theta} + \frac{\partial^2 v_r}{\partial x^2}\right] \\
\frac{\partial w}{\partial t} + v_r\frac{\partial w}{\partial r} + \frac{w}{r}\frac{\partial w}{\partial \theta} + \frac{w v_r}{r} + u\frac{\partial w}{\partial x} &= -\frac{1}{r}\frac{\partial p}{\partial \theta} + \\
&\frac{1}{Re}\left[\frac{\partial}{\partial r}\left(\frac{1}{r}\frac{\partial}{\partial r}(r w)\right) + \frac{1}{r^2}\frac{\partial^2 w}{\partial \theta^2} + \frac{2}{r^2}\frac{\partial v_r}{\partial \theta} + \frac{\partial^2 w}{\partial x^2}\right] \\
\frac{\partial u}{\partial t} + v_r\frac{\partial u}{\partial r} + \frac{w}{r}\frac{\partial u}{\partial \theta} + u\frac{\partial u}{\partial x} &= -\frac{\partial p}{\partial x} + \\
&\frac{1}{Re}\left[\frac{1}{r}\frac{\partial}{\partial r}\left(r\frac{\partial u}{\partial x}\right) + \frac{1}{r^2}\frac{\partial^2 u}{\partial \theta^2} + \frac{\partial^2 u}{\partial x^2}\right]
\end{aligned}
\tag{6.2}
$$

To derive the disturbance equations, each of the velocity vector components is divided into mean and disturbance parts, with the disturbance being of order ϵ. The functional form for the mean part only involves the cross-stream coordinate consistent with the axisymmetric parallel mean flow assumption. Also consistent with the parallel mean flow assumption is the requirement for zero mean radial velocity. The expansions are given in Equations 6.3.

$$
\begin{aligned}
u &= U(r) + \epsilon\tilde{u}(x, r, t) \\
v_r &= \epsilon\tilde{v}_r(x, r, t) \\
w &= W(r) + \epsilon\tilde{w}(x, r, t) \\
p &= \bar{P}(r) + \epsilon\tilde{p}(x, r, t)
\end{aligned}
\tag{6.3}
$$

Equations 6.4 are obtained after substituting the expressions for the components of $\vec{V}$ into the Navier Stokes equations and only considering contributions of first order in ϵ. The contributions of order one by definition satisfy the mean Navier Stokes equations and therefore drop out of the equations. Contributions of order ϵ^2 are ignored in the small disturbance limit.

$$
\begin{gathered}
\frac{\tilde{v}_r}{r}+\frac{\partial \tilde{v}_r}{\partial r}+\frac{1}{r}\frac{\partial \tilde{w}}{\partial \theta}+\frac{\partial \tilde{u}}{\partial x}=0 \\
\frac{\partial \tilde{v}_r}{\partial t}+\frac{W(r)}{r}\frac{\partial \tilde{v}_r}{\partial \theta}+U(r)\frac{\partial \tilde{v}_r}{\partial x}-\frac{2\tilde{w}W(r)}{r}=-\frac{\partial \tilde{p}}{\partial r}+ \\
\frac{1}{Re}\left[\frac{\partial^2 \tilde{v}_r}{\partial r^2}+\frac{1}{r}\frac{\partial \tilde{v}_r}{\partial r}-\frac{\tilde{v}_r}{r^2}+\frac{1}{r^2}\frac{\partial^2 \tilde{v}_r}{\partial \theta^2}+\frac{\partial^2 \tilde{v}_r}{\partial x^2}-\frac{2}{r^2}\frac{\partial \tilde{w}}{\partial \theta}\right] \\
\frac{\partial \tilde{w}}{\partial t}+\frac{W(r)}{r}\frac{\partial \tilde{w}}{\partial \theta}+U(r)\frac{\partial \tilde{w}}{\partial x}+\tilde{v}_r W'(r)+\tilde{v}_r\frac{W(r)}{r}=-\frac{1}{r}\frac{\partial \tilde{p}}{\partial \theta}+ \\
\frac{1}{Re}\left[\frac{\partial^2 \tilde{w}}{\partial r^2}+\frac{1}{r}\frac{\partial \tilde{w}}{\partial r}-\frac{\tilde{w}}{r^2}+\frac{1}{r^2}\frac{\partial^2 \tilde{w}}{\partial \theta^2}+\frac{\partial^2 \tilde{w}}{\partial x^2}+\frac{2}{r^2}\frac{\partial \tilde{v}_r}{\partial \theta}\right] \\
\frac{\partial \tilde{u}}{\partial t}+\frac{W(r)}{r}\frac{\partial \tilde{u}}{\partial \theta}+U(r)\frac{\partial \tilde{u}}{\partial x}+\tilde{v}_r U'(r)=-\frac{\partial \tilde{p}}{\partial x}+ \\
\frac{1}{Re}\left[\frac{\partial^2 \tilde{u}}{\partial r^2}+\frac{1}{r}\frac{\partial \tilde{u}}{\partial r}+\frac{1}{r^2}\frac{\partial^2 \tilde{u}}{\partial \theta^2}+\frac{\partial^2 \tilde{u}}{\partial x^2}+\frac{2}{r^2}\right]
\end{gathered} \tag{6.4}
$$

The next step is to put the disturbance components of velocity into normal mode form. The normal mode forms of the disturbances are given in Equation 6.5. Note that the radial velocity eigenfunction $F(r)$, has a slightly different form. This form is used to obtain a simplify presentation, especially in the continuity equation. The normal mode forms of the perturbation velocity are now substituted into Equation 6.4. The result is a seventh order system of equations consisting of four differential equations, three second order equations and one first order equation. This seventh order system can be converted to a sixth order system using the continuity equation in the radial momentum equation. The sixth order system of equations is given in 6.6.

$$
\{\tilde{v}_r,\tilde{w},\tilde{u},\tilde{p}\}=\{iF(r),G(r),H(r),P(r)\}e^{i(\alpha x-m\theta-\omega t)} \tag{6.5}
$$

$$
\begin{aligned}
&\frac{F}{r} + \frac{mG}{r} + \alpha H + F' = 0 \\
\left[\omega - \alpha U(r) - \frac{mW(r)}{+}\frac{i}{Re}\left(\alpha^2 + \frac{m^2}{r^2}\right)\right] F + \left(\frac{im}{r^2 Re} - \frac{2W(r)}{r}\right) &G+ \\
&\frac{im}{rRe}G' + \frac{i\alpha}{Re}H' + P' = 0 \\
\left[-i\omega + i\alpha U(r) + \frac{imW(r)}{r} + \frac{1}{Re}\left(\alpha^2 + \frac{m^2+1}{r^2}\right)\right] &G+ \\
\left(\frac{2m}{r^2 Re} + \frac{iW(r)}{r} + iW'(r)\right) F - \frac{G'}{rRe} - \frac{G''}{Re} + \frac{imP}{r} &= 0 \\
iU'(r)F + \left[-i\omega + i\alpha U(r) + \frac{imW(r)}{r} + \frac{1}{Re}\left(\alpha^2 + \frac{m^2}{r^2}\right)\right] &H+ \\
-\frac{H'}{rRe} - \frac{H''}{Re} &= 0 \qquad (6.6)
\end{aligned}
$$

The boundary conditions at the centerline for the disturbance quantities depend on the azimuthal wavenumber. The derivation of the boundary conditions here is non-trivial and was originally done by Batchelor and Gill (1962). The equations describing the boundary conditions at the centerline are given in Equations 6.7. For semi-infinite domain calculations, the boundary conditions reduce to a requirement that all disturbance quantities must vanish in the limit of infinite radius. In the case of a wall boundary for the calculations, boundary conditions require that disturbance velocities vanish. The boundary condition for pressure is that it balance the local normal viscous forces. For cylindrical coordinates, the requirement reduces to the radial momentum equation, evaluated at the wall. The wall boundary condition is discussed in detail by Khorrami and Malik (1989). The pressure boundary condition at the wall is given by Equation 6.8.

$$
\begin{aligned}
n = 0 &: F(0) = G(0) = 0 \qquad H'(0) = P'(0) = 0 \\
n = \pm 1 &: F(0) \pm G(0) = 0 \qquad 2F'(0) + nG'(0) = 0 \qquad H(0) = P(0) = 0 \\
|n| > 1 &: F(0) = G(0) = H(0) = P(0) = 0 \qquad (6.7)
\end{aligned}
$$

$$
P_w = \frac{F''_w}{Re} + \frac{F'_w}{Rer_w} \qquad (6.8)
$$

Together with the boundary conditions, the set of equations 6.6 forms an eigenvalue problem where only specific combinations of α and ω give non-trivial solutions to the problem. The eigenfunctions are the radial distributions of the disturbance quantities. The disturbance functions therefore cannot be associated with a specific amplitude and must be viewed as relative. The interpretation of analysis results depends on whether α or ω, or both (using an additional requirement condition) are considered the eigenvalue(s). The interpretation of results is discussed in detail in Section 6.4.

6.3 Linear stability analysis in turbulent flow

To derive the equations for an organized wave disturbance in a turbulent flow, the development by Reynolds and Hussain (1972) is followed very closely. The major difference is the application of the operations performed by Reynolds and Hussain (1972) to the Navier Stokes equations in cylindrical rather than cartesian coordinates.

Reynolds and Hussain (1972) introduced the concept of phase averaging of the equations. The phase average and time average operations are defined in Equation 6.9 and Equation 6.10 respectively.

$$< f(\vec{s},t) > = \lim_{N\to\infty} \frac{1}{N} \sum_{n=0}^{N} f(\vec{s}, t + n\tau) \tag{6.9}$$

$$\overline{f}(\vec{s},t) \ = \lim_{T\to\infty} \frac{1}{T} \int_0^T \ f(\vec{s},t) \tag{6.10}$$

Each function of interest is thus represented by the combination of contributions from the time-average term $\bar{f}$, the phase average term $\tilde{f}$, and from random fluctuations f'. The different operations of averaging applied to these separate contributions and their combined application gives rise to the important relationships given in Equation 6.11, as reported in Reynolds and Hussain (1972). The development here thus is similar to the laminar equations except that the velocity component is divided into three parts and no assumptions are initially made with respect to the magnitude of the wave disturbance.

$$
\begin{aligned}
&< f' >= 0, && \bar{\tilde{f}} = 0, && \overline{f'} = 0, \\
&\overline{\bar{f} g} = \bar{f}\bar{g}, && < \tilde{f} g >= \tilde{f} < g >, && < \bar{f} g >= \bar{f} < g >, \\
&\overline{< f >} = \bar{f}, && < \bar{f} >= \bar{f}, && \overline{\tilde{f} g'} =< \overline{\tilde{f} g'} >= 0.
\end{aligned}
\tag{6.11}
$$

The incompressible continuity equation states that the divergence of the velocity field is to vanish. The divergence operator in cylindrical coordinates is as in cartesian coordinates a linear operator with respect to the flow variables, so that the divergence of the each of the function components described above must vanish individually. The momentum equations for r, θ and x coordinate directions are given again here in Equations 6.12, neglecting body forces such as gravity. The presentation here in Equations 6.12 makes use of the substantial derivative operator defined in Equation 6.13 and is written in terms of the stress tensor components (Panton, 1984).

$$
\begin{aligned}
\frac{D}{Dt}(v_r) &= -\frac{1}{\rho}\frac{\partial p}{\partial r} + \frac{1}{r}\frac{\partial}{\partial r}(r\tau_{rr}) + \frac{1}{r}\frac{\partial}{\partial \theta}(\tau_{r\theta}) + \frac{\partial}{\partial z}(\tau_{rz}) - \frac{\tau_{\theta\theta}}{r} + \frac{w^2}{r} \\
\frac{D}{Dt}(w) &= -\frac{1}{r\rho}\frac{\partial P}{\partial \theta} + \frac{1}{r}\frac{\partial}{\partial r}(r\tau_{\theta r}) + \frac{1}{r}\frac{\partial}{\partial \theta}(\tau_{\theta\theta}) + \frac{\partial}{\partial z}(\tau_{\theta z}) + \frac{\tau_{\theta r}}{r} - \frac{w v_r}{r} \\
\frac{D}{Dt}(u) &= -\frac{1}{\rho}\frac{\partial P}{\partial z} + \frac{1}{r}\frac{\partial}{\partial r}(r\tau_{zr}) + \frac{1}{r}\frac{\partial}{\partial \theta}(\tau_{z\theta}) + \frac{\partial}{\partial z}(\tau_{zz})
\end{aligned}
\tag{6.12}
$$

$$
\frac{D}{Dt}(f) = v_r\frac{\partial}{\partial r}(f) + \frac{w}{r}\frac{\partial}{\partial \theta}(f) + u\frac{\partial}{\partial z}(f) \tag{6.13}
$$

Note that only very few of the terms in the momentum equations are non–linear in the velocity. All the calculations involving the stress tensor are linear operations on the velocities. Writing each velocity component and the pressure as the sum of the time–mean, the organized wave disturbance and the random turbulent contributions and using the relationships of Equations 6.11, the phase averaged and then subsequently time averaged momentum equations may be obtained, as given in Equations 6.14 and Equations 6.15, respectively.

$$
\begin{aligned}
&\frac{D}{Dt}(\tilde{v}_r) + \frac{D}{Dt}(\bar{v}_r) + \frac{G}{Gx}(\bar{v}_r) = -\frac{1}{\rho}\frac{\partial(\bar{p}+\tilde{p})}{\partial r} + \frac{1}{r}\frac{\partial}{\partial r}\left(r(\bar{\tau}_{rr} + \tilde{\tau}_{rr} - \tilde{v}_r^2 - <(v_r')^2>)\right) + \\
&\frac{1}{r}\frac{\partial}{\partial \theta}\left(\bar{\tau}_{r\theta} + \tilde{\tau}_{r\theta} - \tilde{v}_r\tilde{w} - <v_r'w'>\right) + \frac{\partial}{\partial z}\left(\bar{\tau}_{rz} + \tilde{\tau}_{rz} - \tilde{v}_r\tilde{u} - <v_r'u'>\right) \\
&- \frac{\bar{\tau}_{\theta\theta} + \tilde{\tau}_{\theta\theta} - \tilde{w}^2 - <(w')^2>}{r}
\end{aligned}
$$

$$
\begin{aligned}
&\frac{D}{Dt}(\tilde{w}) + \frac{D}{Dt}(\bar{w}) + \frac{G}{Gx}(\bar{w}) = -\frac{1}{r\rho}\frac{\partial(\bar{p}+\tilde{p})}{\partial \theta} + \frac{1}{r}\frac{\partial}{\partial r}\left(r(\bar{\tau}_{\theta r} + \tilde{\tau}_{\theta r} - \tilde{w}\tilde{v}_r - <w'v_r'>)\right) + \\
&\frac{1}{r}\frac{\partial}{\partial \theta}\left(\bar{\tau}_{\theta\theta} + \tilde{\tau}_{\theta\theta} - \tilde{w}^2 - <(w')^2>\right) + \frac{\partial}{\partial z}\left(\bar{\tau}_{\theta z} + \tilde{\tau}_{\theta z} - \tilde{w}\tilde{u} - <w'u'>\right) \\
&+ \frac{\bar{\tau}_{\theta r} + \tilde{\tau}_{\theta r} - \tilde{w}\tilde{v}_r - <w'v_r'>}{r}
\end{aligned}
$$

$$
\begin{aligned}
&\frac{D}{Dt}(\tilde{u}) + \frac{D}{Dt}(\bar{u}) + \frac{G}{Gx}(\bar{u}) = -\frac{1}{\rho}\frac{\partial(\bar{p}+\tilde{p})}{\partial z} + \frac{1}{r}\frac{\partial}{\partial r}\left(r(\bar{\tau}_{zr} + \tilde{\tau}_{zr} - \tilde{u}\tilde{v}_r - <u'v_r'>)\right) + \\
&\frac{1}{r}\frac{\partial}{\partial \theta}\left(\bar{\tau}_{z\theta} + \tilde{\tau}_{z\theta} - \tilde{u}\tilde{w} - <u'w'>\right) + \frac{\partial}{\partial z}\left(\bar{\tau}_{zz} + \tilde{\tau}_{zz} - \tilde{u}^2 - <(u')^2>\right)
\end{aligned}
$$

$$
\frac{G}{Gx}(\bar{f}) = \tilde{v}_r\frac{\partial}{\partial r}(\bar{f}) + \frac{\tilde{w}}{r}\frac{\partial}{\partial \theta}(\bar{f}) + \tilde{u}\frac{\partial}{\partial z}(\bar{f}) \tag{6.14}
$$

$$
\begin{aligned}
&\frac{D}{Dt}(\bar{v}_r) = -\frac{1}{\rho}\frac{\partial \bar{p}}{\partial r} + \\
&\frac{1}{r}\frac{\partial}{\partial r}\left(r(\bar{\tau}_{rr} - \overline{\tilde{v}_r^2} - \overline{(v_r')^2})\right) + \frac{1}{r}\frac{\partial}{\partial \theta}\left(\bar{\tau}_{r\theta} - \overline{\tilde{v}_r\tilde{w}} - \overline{v_r' w'}\right) + \frac{\partial}{\partial z}\left(\bar{\tau}_{rz} - \overline{\tilde{v}_r\tilde{u}} - \overline{v_r' u'}\right) \\
&-\frac{\bar{\tau}_{\theta\theta} - \overline{\tilde{w}^2} - \overline{(w')^2}}{r}
\end{aligned}
$$

$$
\begin{aligned}
&\frac{D}{Dt}(\bar{w}) = -\frac{1}{r\rho}\frac{\partial \bar{p}}{\partial \theta} + \\
&\frac{1}{r}\frac{\partial}{\partial r}\left(r(\bar{\tau}_{\theta r} - \overline{\tilde{w}\tilde{v}_r} - \overline{w' v_r'})\right) + \frac{1}{r}\frac{\partial}{\partial \theta}\left(\bar{\tau}_{\theta\theta} - \overline{\tilde{w}^2} - \overline{(w')^2}\right) + \frac{\partial}{\partial z}\left(\bar{\tau}_{\theta z} - \overline{\tilde{w}\tilde{u}} - \overline{w' u'}\right) \\
&+\frac{\bar{\tau}_{\theta r} - \overline{\tilde{w}\tilde{v}_r} - \overline{w' v_r'}}{r}
\end{aligned}
$$

$$
\begin{aligned}
&\frac{D}{Dt}(\bar{u}) = -\frac{1}{\rho}\frac{\partial \bar{p}}{\partial z} + \\
&\frac{1}{r}\frac{\partial}{\partial r}\left(r(\bar{\tau}_{zr} - \overline{\tilde{u}\tilde{v}_r} - \overline{u' v_r'})\right) + \frac{1}{r}\frac{\partial}{\partial \theta}\left(\bar{\tau}_{z\theta} - \overline{\tilde{u}\tilde{w}} - \overline{u' w'}\right) + \frac{\partial}{\partial z}\left(\bar{\tau}_{zz} - \overline{\tilde{u}^2} - \overline{(u')^2}\right)
\end{aligned}
\tag{6.15}
$$

To obtain the dynamic equations for the organized wave disturbance, subtract Equations 6.15 from Equations 6.14. The resulting system is given in Equations 6.16. Together with the continuity equation for the wave disturbance component of the velocity, Equations 6.16 describe the behaviour of an organized wave disturbance in a turbulent flow. One interesting aspect of Equation 6.16 is the appearance of a difference of averages in Reynolds stresses, $\overline{(v_r')^2} - < (v_r')^2 >$ for example. The difference between the time average and phase average of the Reynolds stress replaces the original closure problem in turbulent flow modeling.

$$
\begin{aligned}
&\frac{D}{Dt}(\tilde{v}_r)+\frac{G}{Gx}(\bar{v}_r)=-\frac{1}{\rho}\frac{\partial\tilde{p}}{\partial r}+\frac{1}{r}\frac{\partial}{\partial r}\Big(r(\tilde{\tau}_{rr}+(\overline{\tilde{v}_r^2}-\tilde{v}_r^2)+(\overline{(v_r')^2}-<(v_r')^2>))\Big)+\\
&\frac{1}{r}\frac{\partial}{\partial\theta}\left(\tilde{\tau}_{r\theta}+(\overline{\tilde{v}_r\tilde{w}}-\tilde{v}_r\tilde{w})+(\overline{v_r'w'}-<v_r'w'>)\right)+\frac{\partial}{\partial z}\left(\tilde{\tau}_{rz}+(\overline{\tilde{v}_r\tilde{u}}-\tilde{v}_r\tilde{u})+(\overline{v_r'u'}-<v_r'u'>)\right)\\
&-\frac{\tilde{\tau}_{\theta\theta}+(\overline{\tilde{w}^2}-\tilde{w}^2)+(\overline{(w')^2}-<(w')^2>)}{r}
\end{aligned}
$$

$$
\begin{aligned}
&\frac{D}{Dt}(\tilde{w})+\frac{G}{Gx}(\bar{w})=-\frac{1}{r\rho}\frac{\partial\tilde{p}}{\partial\theta}+\frac{1}{r}\frac{\partial}{\partial r}\left(r(\tilde{\tau}_{\theta r}+(\overline{\tilde{w}\tilde{v}_r}-\tilde{w}\tilde{v}_r)+(\overline{w'v_r'}-<w'v_r'>)\right)+\\
&\frac{1}{r}\frac{\partial}{\partial\theta}\Big(\tilde{\tau}_{\theta\theta}+(\overline{\tilde{w}^2}-\tilde{w}^2)+(\overline{(w')^2}-<(w')^2>)\Big)+\frac{\partial}{\partial z}\left(\tilde{\tau}_{\theta z}+(\overline{\tilde{w}\tilde{u}}-\tilde{w}\tilde{u})+(\overline{w'u'}-<w'u'>)\right)\\
&+\frac{\tilde{\tau}_{\theta r}+(\overline{\tilde{w}\tilde{v}_r}-\tilde{w}\tilde{v}_r)+(\overline{w'v_r'}-<w'v_r'>)}{r}
\end{aligned}
$$

$$
\begin{aligned}
&\frac{D}{Dt}(\tilde{u})+\frac{G}{Gx}(\bar{u})=-\frac{1}{\rho}\frac{\partial\tilde{p}}{\partial z}+\frac{1}{r}\frac{\partial}{\partial r}\left(r(\tilde{\tau}_{zr}+(\overline{\tilde{u}\tilde{v}_r}-\tilde{u}\tilde{v}_r)+(\overline{u'v_r'}-<u'v_r'>))\right)+\\
&\frac{1}{r}\frac{\partial}{\partial\theta}\left(\tilde{\tau}_{z\theta}+(\overline{\tilde{u}\tilde{w}}-\tilde{u}\tilde{w})+(\overline{u'w'}-<u'w'>)\right)+\frac{\partial}{\partial z}\Big(\tilde{\tau}_{zz}+(\overline{\tilde{u}^2}-\tilde{u}^2)+(\overline{(u')^2}-<(u')^2>)\Big)
\end{aligned}
$$

$$
\frac{G}{Gx}(\bar{f})=\tilde{v}_r\frac{\partial}{\partial r}(\bar{f})+\frac{\tilde{w}}{r}\frac{\partial}{\partial\theta}(\bar{f})+\tilde{u}\frac{\partial}{\partial z}(\bar{f})
\tag{6.16}
$$

The interpretation of terms such as $\overline{(v_r')^2}-<(v_r')^2>$ as stresses is facilitated by presenting the equations using the stress tensor components. Each laminar stress tensor component has a turbulent analog. The closure problem must now be addressed. As a first step, the disturbance wave is assigned a small magnitude ϵ similar to the development for the laminar disturbance equations. The nonlinear terms in the disturbance wave velocity now can be dropped from the equation in the small disturbance limit.

Reynolds and Hussain (1972) discuss several possibilities of first order closure for the disturbance stresses (e.g. $\overline{(v_r')^2}-<(v_r')^2>$). Under the assumption that the turbulent energy and time scale remain unchanged in the presence of the disturbance wave, a closure model exactly analogous to the turbulent viscosity model is obtained. With this closure model, the disturbance stresses are absorbed into the a cumulative stress tensor. The resulting equations are identical to the laminar disturbance equations, except that the Reynolds number must be viewed as a turbulent Reynolds number based on $\nu_t + \nu$ the sum of the laminar and turbulent kinematic viscosities. The closure problem is not completely solved because the turbulent viscosity must still be specified. However, since the turbulent energy and time scale are assumed independent of the disturbance, the turbulent viscosity is completely determined by mean flow turbulence characteristics. Equation 6.17 shows the equation for the turbulent viscosity in terms of the turbulent kinetic energy and the turbulence length scale. An equivalent formulation using a turbulent time scale is also given in Equation 6.17.

$$\nu_t = c_t \sqrt{k} l_m = c_t k t_t \tag{6.17}$$

The value of c is found to be around 0.5 from experimental measurements (Pope, 2001). The model used for the turbulent viscosity is still not completely defined even using an estimate for the turbulent kinetic energy from experiments. The length scale or time scale associated with the turbulent fluctuations must still be determined. The analysis reported below will not rigourously fix ν_t. Rather, the influence of the distribution and magnitude of ν_t will be examined using the basic model given in Equation 6.18. The model essentially accounts for the typical distribution of turbulent kinetic energy encountered in the flows studied here. The overall multiplying factor $sqrtkl_m$ can be viewed as the product of an average length scale and the square root of the mean turbulent kinetic energy for the flow. The model constant, d can be chosen to change the relative maxima of the model turbulent kinetic energy distribution. The model constant dd is chosen to be an even integer. The higher its magnitude, the narrower the distribution maxima.

$$\nu_t = c_t k l_m \left(\cos^d d \left[\pi \frac{r - R_i}{R - R_i} \right] e^{-dd * r^2} \right) \tag{6.18}$$

Based on the data already presented, several short comings of the model implemented must be pointed out at this point. The most fundamental short-coming is that the model used is derived assuming isotropic turbulence and as a result, the influence of anisotropy on the stability of the flow field cannot be studied. A second short-coming, specific to the turbulent viscosity model used is that the boundary layer distribution of turbulent kinetic energy near walls is not captured.

Nevertheless, the model developed here represents a significant step forward in the analysis of the stability of swirling flows. The model allows the effects of a radially variable viscosity on the stability of a flow field to be examined.

6.4 Interpretation of results

The interpretation of analysis results depends on how the governing equations are solved. Three types of analysis will be described. The analysis making the complex frequency ω the eigenvalue while fixing the axial wavenumber α is called a temporal stability analysis. On the other hand, if ω is fixed and α is the eigenvalue, a spatial stability analysis is performed. If the relationship between α and ω is restricted such that the combination of both values defines a point of vanishing group velocity, the resulting analysis determines the absolute stability of the flow field.

6.4.1 Description of instability analysis types

In temporal stability analysis, the disturbance is applied in space (by the fixed wavenumber α) and is observed as it evolves in time (through the complex frequency ω calculated as the eigenvalue). In a temporal stability analysis, stability of the flow is indicated by all eigenvalues having negative imaginary parts. The imaginary part of the frequency thus defines the linear growth rate of the disturbance whereas the real part defines the circular frequency. Temporal stability analysis was the first type of linear stability analysis performed in flows, in part because computationally, these calculations are less taxing.

Spatial stability analysis has received most of the attention in literature. The disturbance is applied in time (with real frequency ω) and the evolution of the disturbance is observed in space. Spatial stability analysis results can thus be easily compared to experimental results where usually the flow is excited at a point and effect of the excitation is studied as the flow evolves downstream. Early on, transformations of growth rates were performed that made it possible to compare temporal stability analysis results with spatial stability results. However, Gaster (1962) showed that the transformation is only valid for small growth rates and hence spatial stability analysis is most common for free shear layer stability analysis.

In addition to these stability analysis types, absolute stability analysis is an important analysis. An absolutely unstable flow field will not allow excitation of any other modes and instead behave like a self-excited oscillator. To determine absolute stability, all points with vanishing complex group velocity are found. If any of these points are found to have a positive temporal growth rate, the flow is absolutely unstable. The saddle point condition is expressed mathematically in Equation 6.19.

$$\frac{d\omega}{d\alpha}(\alpha_o) = 0 \qquad with \qquad \omega_o = \omega(\alpha_o) \tag{6.19}$$

An expansion around the saddle point (branch point in complex α and ω space) can be shown to have second order form. The mathematical expansion near the saddle point is given by Equation 6.20. The coefficients s_fit and l_fit are complex and depend on the exact makeup of the saddle point. Figure 6.1 shows a 3-D plot of Equation 6.20. Both positive and negative branches of wavenumber are plotted for a range of complex frequencies.

$$\alpha^{\pm} - \alpha_o = \pm s_{fit}\sqrt{\omega - \omega_o} + l_{fit}(\omega - \omega_o) \tag{6.20}$$

Equation 6.20 can be used to help predict the saddle point location and verify that the branch point is the result of the coalescence of an upstream and downstream spatial modes. An upstream mode is a mode whose group velocity for a large enough temporal growth rate is negative with respect to the flow direction. A downstream mode is a mode whose group velocity is positive at some large enough temporal growth rate. As the temporal growth rate $imag(\omega)$ is decreased the upstream mode will have increasing group velocity and the downstream mode will have decreasing group velocity. At the branch point the group velocity is zero and energy grows in place.

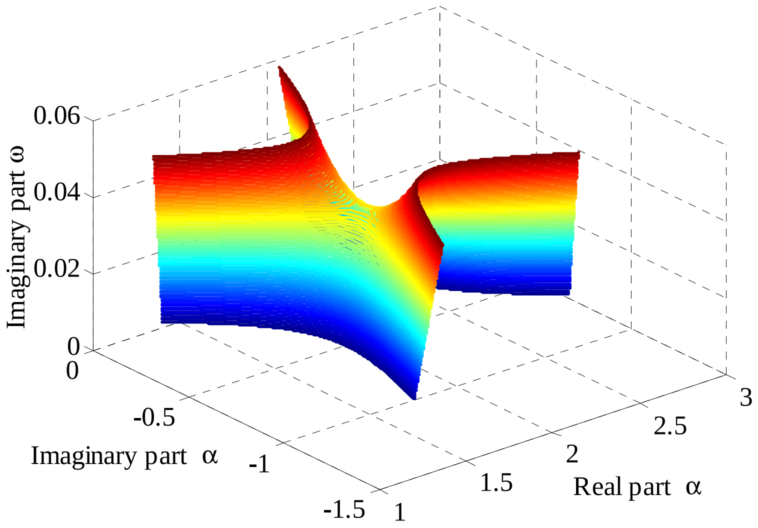

Figure 6.1: 3-D plot of saddle constructed from model branches around a saddle point

An example showing the quality of the fit achieved using Equation 6.20, is given in Figure 6.2. The model captures the dependence the structure of the two branches very well, whether the growth rate estimate is too high or too low. The error in the estimate increases with distance from the saddle point, as expected. Section 6.5.3 discusses the actual procedure used to obtain the saddle point.

6.5 Solution methods

Various methods of solving the eigenvalue problem represented by the governing linear instability equation (Equations 6.6, for example) have been used. The most common methods are shooting and Chebychev collocation methods. The shooting method offers the advantage of being able to assess parametric variations of modes very easily whereas the initial calculation of an eigenvalue is more difficult and the speed of solution strongly depends on the quality of the initial guess. The Chebychev collocation method offers the advantage that in one calculation a whole set of eigenvalues is explicitly calculated (without iteration), but parametric variations are

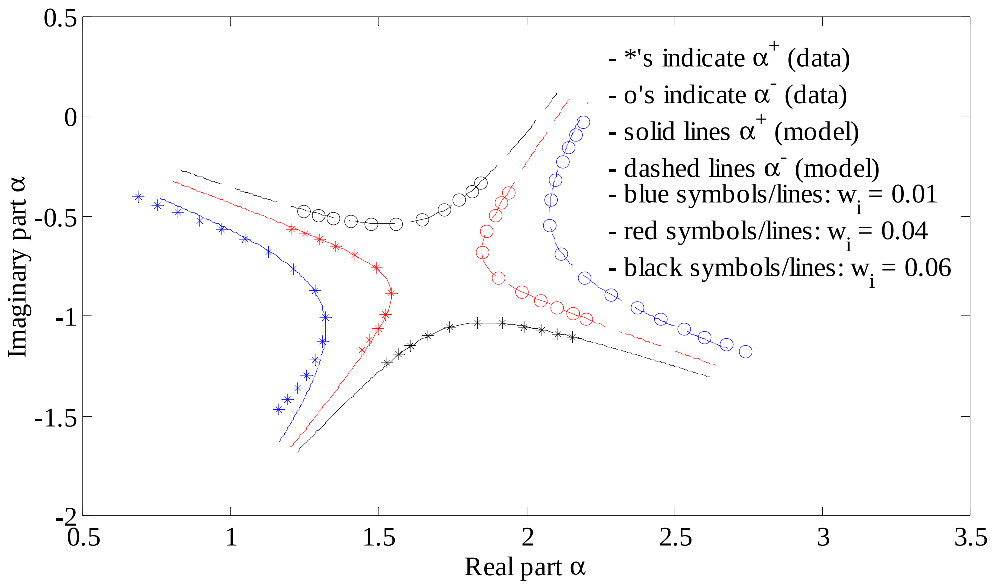

Figure 6.2: Calculated and modeled branches around a saddle point

more difficult and time consuming, considering that each calculation gives an entire spectrum of eigenvalues even though only one mode is generally of interest.

6.5.1 Shooting method implementation

The shooting method has been used by Nachtsheim (1964), for example, for the solution of the Orr-Sommerfeld equation and Morris (1976), for example, for the solution of the axisymmetric disturbance equations without swirl. In each case an important hurdle to overcome is the search for all relevant eigenvalues, to assure that the least stable mode has in fact been computed. The most often used method is that introduced by Lessen et al. (1968) in their study of the stability of pipe Poiseuille flow. The method consists of calculating the net number of times the phase of the determinant of the problem matrix changes by 2π over any closed contour in the complex eigenvalue plane. The number of complete phase changes is equal to the number of eigenvalues contained in the contour. In this manner, it is possible to assure that the least stable eigenvalue for a given problem has been found. The method is not restricted to viscous flow stability problems and has been used for inviscid calculations by Michalke (1999) for example.

The shooting method is implemented in the numerical analysis package MATLAB (1999). The shooting method has the capability of calculating both axisymmetric and 2-D linear parallel stability problems. Using the boundary conditions, three linearly independent solutions near r=0 are found. These three solutions are integrated together to a radius where the solution is then matched to the asymptotic expansion for large radius or the wall boundary conditions, depending on the problem. The integration routine used is implemented in C code and can be called from MATLAB (1999) using the application program interface (API). The integration method used is taken from Press et al. (1992) and called Bullrisch-Stoer. Bullrisch-Stoer is a variable step variable order integration technique that is based on the modified midpoint method. The integration step is divided into, say, 4, 6 and 8 sub-intervals over which a modified midpoint integration is performed. The results are then extrapolated to infinitely many sub-intervals to obtain excellent accuracy. The method checks its efficiency and adjusts either the number of midpoint integrations or the interval size depending on the convergence achieved at the last step. In the process of integration the solution vector magnitude of each solution is checked to see if a threshold value is exceeded (e.g. 10^7). If the threshold is exceeded a Gram-Schmidt ortho-normalization of the three solution vectors is performed.

The integration ends either at the location where wall boundary conditions are to be enforced or at an appropriately large radius (usually around r = 4) where the asymptotic solutions to the disturbance equations are evaluated in the case of a semi–infinite domain.

Both wall boundary conditions and the solution to the asymptotic expansion admit three linearly independent solutions which must be matched to the three vectors that form the result of the integration. These six solution vectors each have six elements describing the unknowns at the matching point. The unknowns are the disturbance quantities and the derivatives of the azimuthal and axial disturbance quantities (the unknowns are: F, G, G', H, H' and P). The shooting method attempts to drive the determinant of this matrix (6x6) to zero by changing the eigenvalue (either α or ω - see Section 6.4). The new trial values are determined using a damped Newton algorithm. The Jacobian required for the Newton algorithm is obtained by numerical perturbation of the eigenvalue.

The calculation of the solution expansions near the centerline and at large radius deserve further discussion. The inner radius expansions required for the solution of axisymmetric stability problems are solved to eighth order by the method of Frobenius (Bender and Orszag, 1978). The power expansion is setup as shown in Equation 6.21. The indicial equation is obtained from the characteristic equation of the determinant of the matrix operator representing the governing sixth order differential equation. The six roots of the indicial equation are found to be $\pm(n+1), \pm(n-1), \pm n$. Of the six roots, three must be excluded because they become ill-defined in the limit as r approaches zero. The remaining three solutions can all be obtained by using $\lambda_f = n+1$. After setting $\lambda_f = n+1$, power expansions for the disturbance quantities (Equation 6.21) and mean flow profiles are substituted into the governing equations. The equations are then solved for each power of r individually. For the calculations presented here, the expansions were carried out to sixth order. For most calculations, the solution integration was started at r=0.005.

$$s(r) = r^{\lambda_f} \sum_{j=0}^{\infty} s_j r^j \tag{6.21}$$

A similar procedure is used for the expansions at large radius. For zero mean velocity, the governing equations can be solved in closed form in terms of Bessel functions. To stay general however and allow for slow mean velocity decay, another power expansion is formulated here. Formally, the expansion can be calculated according to the method of Wasow (Lessen and Paillet, 1974). However, as shown by Lessen and Paillet (1974), the same result can be arrived at by formulating a power expansion in the form of Equation 6.22 and determining the unknown λ_{w1} and λ_{w1} by requiring non-trivial solutions. For the sixth order differential equation system studied here, the eigenvalue problems that result after substituting Equation 6.22 require that λ_{w2} is equal to $-1/2$. Six possible values for λ_{w1} are found: $\pm\alpha \pm \sqrt{alpha^2 - I * omega * Rey}(twice)$. For each α and ω, three of the six roots will give solutions that vanish as r goes to infinity as required by the boundary conditions. When one of the repeated pair of eigenvalues is substituted into the equations, two expansion constants will remain independent to give a total of three linearly independent solutions.

$$s(r) = e^{\lambda_{w1} r} r^{\lambda_{w2}} \sum_{j=0}^{\infty} \frac{s_j}{r^j} \tag{6.22}$$

It should be mentioned separately that the expansion calculations described here closely follow the development of Lessen and Paillet (1974).

6.5.2 Chebychev collocation method implementation

Chebychev methods have been used by Orszag (1971); Zebib (1987); Huang et al. (1994); Khorrami (1991) in entirely different applications. Orszag (1971) studied the Orr-Sommerfeld equations for 2-D Poiseuille flow. Zebib (1987) studied the global stability of flow past a circular cylinder. Huang et al. (1994) studied a swirling elliptical jet with combustion. Khorrami (1991) studied the trailing line (Batchelor) vortex. The same authors published an elegant paper (Khorrami and Malik, 1989) that gives extensive details on the application of the method. These details are summarized here because although the shooting method is very common in a wide variety of applications, the Chebychev method is less common and deserves more detailed discussion.

The Chebychev method or more precisely the Chebychev collocation method is based on the Chebychev polynomial, defined on the interval [-1,1] and for the k$^t h$ polynomial in Equation 6.23. To implement the method it can be shown that satisfying the differential equation exactly at certain points in the Chebychev domain [-1,1] yields a convergent solution of the differential equation in the entire Chebychev domain. The chosen points are called the collocation points. The most commonly chosen points are the Gauss-Lobatto points: $\xi_j = cos(\Pi j/N)$ with j = 0,1,. . . ,N. At these points the Chebychev polynomials have a simple form: $T_k(\xi_j) = cos(\Pi kj/N)$. Derivatives at each point j can be calculated using recurrence relations (Press et al., 1992).

$$T_k(\xi) = cos\left[kcos^{-1}(\xi)\right] \tag{6.23}$$

The solution vector is given by Equation 6.24, the sum of the contributions of all polynomials in the series. Note that number of polynomials is equal to the number of collocation points. Using recurrence relations for the derivatives the only unknowns remaining in the problem are the coefficients of the k$^t h$ polynomial in each variable. The calculation of these coefficients involves the solution of a matrix R(N+1) x R(N+1) in size (R stands for the number of unknown variables, 6 in the case of the axisymmetric viscous stability equations). The result is a generalized eigenvalue problem that can be treated with many different available algorithms to find the eigenvalues and corresponding eigenvectors. Finally, note that mapping functions are required to map the physical domain into the Chebychev domain $[-1, 1]$. Stretched mappings are used for semi–infinite domain calculations and linear mappings are used for finite domain calculations.

$$\mathbf{Q}(\xi) = \sum_{k=0}^{N} \mathbf{a_k} T_k(\xi) \tag{6.24}$$

The Chebychev collocation method is also implemented in MATLAB (1999). The application of boundary conditions is much more straightforward since neither asymptotic nor near axis expansions are required. The boundary conditions give equations involving all the unknown coefficients for each of the Chebychev polynomials. Similarly the interior equations involve the same coefficients. A generalized eigenvalue problem of the form given in Equation 6.25 is obtained by putting all the terms involving the eigenvalue on the right hand side of the equation. It should be mentioned that the original seventh order system is used here as given in Equations 1.5 to 1.8. The matrix operations involved in setting up the problem in sixth order form are cumbersome enough to forgo the increase in speed gained in actual eigenvalue calculation (Khorrami and Malik, 1989).

$$D\mathbf{Q} = \Lambda E\mathbf{Q} \tag{6.25}$$

In reviewing the governing equations for the axisymmetric viscous stability problem given in Equations 1.5 to 1.8, it is seen that there is an additional difficulty in the calculation of spatial stability. The eigenvalue in this case is α and it occurs to the second power in several of the equations. This circumstance makes the definition of the matrix E in Equation 6.25 difficult. The solution is to define several additional unknowns, $\bar{F} = \alpha F$, $\bar{G} = \alpha G$ and $\bar{H} = \alpha H$. Adding these equations to the other governing equations increases the number of unknowns from 4(N+1) to 7(N+1), a significant additional expense in memory requirement and computational time. The same method was implemented by Khorrami and Malik (1989).

The eigenvalue problem is now set, except that the eigenvalue matrix E is singular because the boundary conditions do not involve the eigenvalue (neither α nor ω). To proceed the ranks of both DD and E are reduced (Khorrami and Malik, 1989). The problem is set up in the matrix relation given in Equation 6.26.

$$\begin{bmatrix} D_{11} & D_{12} \\ D_{21} & D_{22} \end{bmatrix} \begin{bmatrix} \mathbf{Q}_1 \\ \mathbf{Q}_2 \end{bmatrix} = \lambda \begin{bmatrix} E_{11} & E_{12} \\ 0 & 0 \end{bmatrix} \begin{bmatrix} \mathbf{Q}_1 \\ \mathbf{Q}_2 \end{bmatrix} \tag{6.26}$$

The bottom row matrix equation given in 6.26 can be solved for part of the unknown vector, $\mathbf{Q}_2$. Having solved for $\mathbf{Q}_2$, the result can be plugged back into the equations to obtain a system of the same form as Equation 6.25 but with DD and E replaced by $\tilde{DD}$ and $\tilde{E}$ respectively, as given in Equation 6.27.

$$\begin{aligned} \tilde{D} &= D_{11} - D_{12} D_{22}^{-1} D_{21} \\ \tilde{E} &= E_{11} - E_{12} D_{22}^{-1} D_{21} \end{aligned} \tag{6.27}$$

One of the reasons the Chebychev method was implemented using MATLAB (1999) is that the software is particularly efficient in matrix manipulation and contains a very efficient solver for the generalized eigenvalue problem described by Equation 6.25. Additionally, complex number arithmetic is handled very well by the software and did not require any special programming strategies (as for example in the C implementation of the integration routine used in the shooting method).

Once the solution and eigenvectors are determined the calculated modes are ordered by their ability to provide a solution to the disturbance equations at points in between the collocation points. By definition the residual of the equations is zero only exactly at the collocation points. Using this method helps in separating spurious eigenvalues from real, physical eigenvalues. In general the spurious eigenvalues turn out to be physical eigenvalues whose value has not yet converged because not enough collocation points were used to properly resolve the eigenfunctions. It should be noted that unstable modes usually have a simpler structure (Morris, 1976) and therefore unstable eigenvalues are the first to converge as the number of collocation points is increased. Lack of convergence of unstable modes can be attributed in most cases to an inappropriate mapping of the physical domain into the Chebychev domain. It is important that the mapping cluster the points where they are needed to resolve the anticipated eigenfunction properly. In free shear flows, the points should be clustered around the area of maximum shear because this area will also likely exhibit the highest amplitude of the eigenfunction. The two mapping types most commonly used are given in Equations 6.28 and 6.29. Equation 6.28 is a linear mapping, evenly spacing the points in the physical domain. Equation 6.29 is a nonlinear mapping which places approximately half the collocation points in the physical domain at $r < a_q$.

$$\xi = 1 - 2r \tag{6.28}$$

$$\xi = \frac{a_q - b_q r}{a_q + r} \quad \text{with} \quad b_q = 1 + \frac{2a_q}{r_{max}} \tag{6.29}$$

6.5.3 Absolute stability analysis implementation

To find the saddle points determining absolute instability as given in Equation 6.19, the shooting method (Section 6.5.1) is used because it is best suited for smooth variations in parameters. The upstream and downstream branches required for the 'pinching condition' are identified using the Chebychev analysis (Section 6.5.2). Once identified, an external damped Newton algorithm is used to drive the group velocity to zero, with some help in determining the approximate saddle point location from a fit to the expansion around the saddle point (Equation 6.20). Estimates of the local group velocity are obtained by central difference and multiple calls to the shooting method to obtain eigenvalues at different parameter values. Note that for the absolute instability analysis both ω and α must be considered complex. However, neither the shooting method nor the Chebychev method is sensitive to this issue, because both were designed to perform temporal (real α) and spatial (real ω) linear stability calculations.

6.5.4 General procedure for linear stability analysis of a local profile

With the tools above in place, it is possible to describe the analysis of a new velocity profile from the outset. The velocity profiles are assumed to be given as continuous functions either from a fit to experiments or an analytical model. At the outset, the profiles are normalized by a suitable measure of the axial velocity (maximum or area mean), and the spatial coordinate is also scaled by the reference dimension. In this way the results can be easily generalized. The frequency and wavenumber used in the calculation are thus also non–dimensional. Asymptotic and inner expansions of the velocity profiles are then determined using polynomial fits and series expansions near the centerline and at large radius respectively. Once the coefficients of the expansions have been obtained, the profile functions (and the derivatives) are entered into the mean flow function written in MATLAB (1999) for access by the Chebychev program.

A reasonable Reynolds number for the flow is chosen together with a range of real frequencies (ω) or wavenumbers (α) for spatial or temporal analysis respectively. Generally the spatial analysis is preferred in free shear layers because of the large growth rates encountered in these flows (see Section 1.4.2) and the more straightforward physical interpretation (see Section 6.4). The Chebychev program is then called to run through the parameter variation prescribed. The parameter space is only superficially investigated to minimize the computational expense for a parameter variation using the Chebychev analysis. The results of the Chebychev analysis are given in the form of eigenvalues and eigenvectors as a function of the selected parameter values, sorted by residuals as described above.

To obtain a glimpse of how a mode varies with the parameter, it is necessary to find a way to relate an eigenvalue at one parameter value to the eigenvalue of the same mode at another parameter value. To perform this task an eigenvalue of interest is chosen at some parameter value. A program was written to compare the eigenvalue of interest and associated eigenfunction to the first N eigenvalues and associated eigenfunctions at the next parameter value. The number N can be chosen depending on the problem and usually is less than 30. Recall that the list is ordered according to the residuals of the solutions. The comparison of eigenfunctions is based on the thought that these vary greatly from mode to mode but only slightly from one parameter value to the next. In this manner initial assessments about the stability of the flow can be made.

Next, the expansions found above for the mean flow are entered into the routines that calculate the expansions for the disturbance quantities near the centerline and in the far–field (if applicable) for the shooting method. An eigenvalue and associated parameter value from the Chebychev analysis is chosen as the initial guess for the shooting method. The entire parameter space of Reynolds number and wavenumber (for example) can be mapped out starting from this single initial guess. The shooting method will however only be able to perform this task for one mode at a time. Once the parameter space is mapped out for all modes of interest a relatively complete picture of stability is formed. The Chebychev analysis will have shown the existence of upstream and downstream branches if they exist, and the shooting method will have thoroughly defined the variation of the growth rate and wavenumber (or frequency) with for example Reynolds number or swirl strength.

If upstream and downstream branches are observed in the Chebychev analysis, an absolute instability analysis is started and the shooting method is used to find the variation of the absolute growth rate and frequency with Reynolds number, swirl strength or some other parameter (the parameter could also be the axial coordinate if the velocity profiles are parameterized in it). To investigate the eigenfunction of a mode at a certain point in parameter space a Chebychev analysis is performed because eigenfunction information is much more easily extracted from that analysis than from the shooting method because of the orthonormalizations performed along the integration path in the shooting method. The use of both Chebychev and shooting methods in the determination of stability characteristics limits the likelihood that a numerical eigenvalue (with no physical meaning) is mistaken for an interesting stability characteristic.

6.6 Benchmark flow stability calculations

The results presented in this section deal mainly with the duplication and extension of published local parallel linear stability studies. The first results presented are for a jet near its exit. The form of the profile is given in Equation 6.30, similar to Morris (1976), Profile II.

$$U(r) = \frac{1}{2}\left(1 + tanh\left[\frac{1}{4\theta_{sl}}\left(\frac{1}{r} - r\right)\right]\right) \tag{6.30}$$

Figure 6.3 shows the velocity profile of the type given in Equation 6.30 analyzed to obtain the results presented in Figures 6.4 to 6.7. Figure 6.4 shows the variation of spatial growth rate with real frequency for several Reynolds numbers and azimuthal mode m=1. The shear layer thickness, θ_{sl} used in these calculations is equal to 0.16. The characteristic dependence of amplification rate with Reynolds number is observed, where the higher the Reynolds number, the higher the amplification rate. Note that as Reynolds number is increased, the location of the frequency for maximum

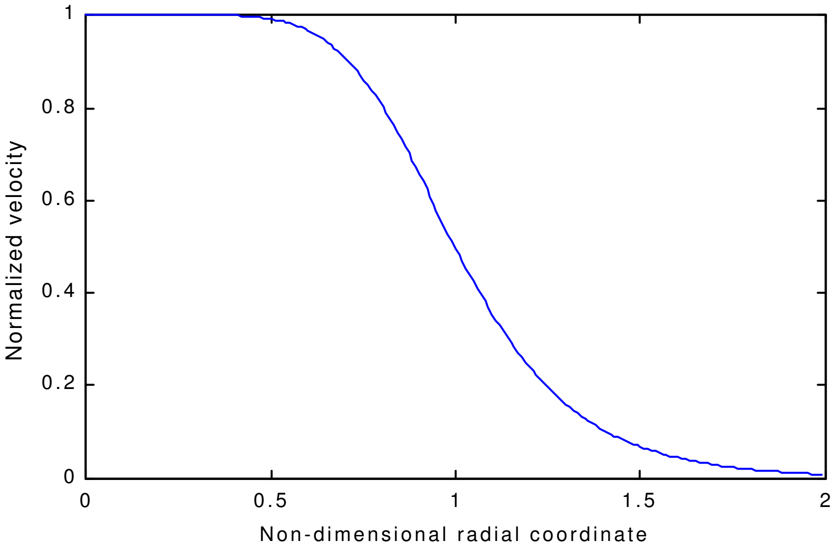

Figure 6.3: Tanh jet profile analyzed for Figures 6.4 to 6.7

growth increases. Plots like these are partly justification for using inviscid analysis for early jet development.

Figure 6.5 shows the normalized real part of the eigenfunctions for one particular case shown in Figure 6.4. The eigenfunctions shown are at a Reynolds number of 250 and a real frequency of 1. The eigenfunctions are normalized by the magnitude of the real part of the radial disturbance velocity magnitude. From Figure 6.5 it becomes immediately clear that the bulk of the disturbance energy is contained as expected in the axial velocity disturbance eigenfunction (H). Note also that most of the activity in the eigenfunction occurs in the area of maximum shear of the analyzed velocity profile, as discussed earlier in Section 6.5.2. Furthermore, the structure of the eigenfunctions is relatively simple, as also noted by Morris (1976).

Figures 6.6 and 6.7 show the behavior of the stability under the same conditions but for the axisymmetric (m=0) mode. Figure 6.6 shows the growth rate and Figure 6.7 shows the real wavenumber. The growth rates observed are comparable to the growth rates seen for the first azimuthal mode, underlining the competition that

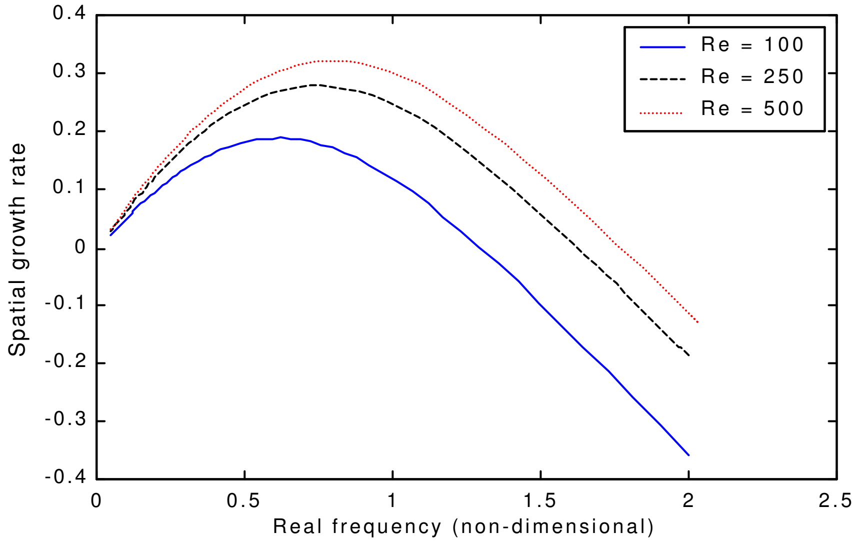

Figure 6.4: Plot of spatial growth rate as a function of real frequency for the tanh jet profile for three Reynolds numbers with m = 1

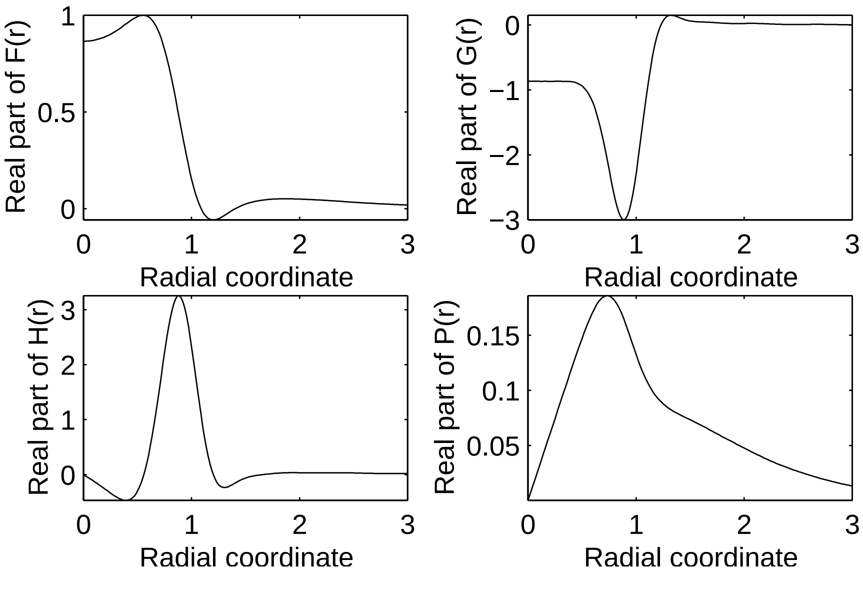

Figure 6.5: Plot of the least stable eigenfunction in the tanh jet for the case $\alpha = 1$, m=1, Re = 250

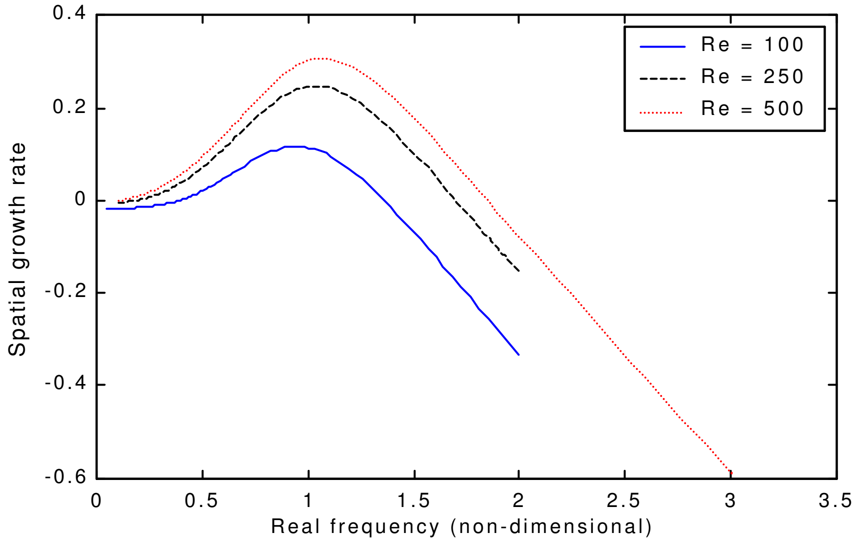

Figure 6.6: Plot of spatial growth rate as a function of real frequency for the tanh jet profile for three Reynolds numbers with m = 0

occurs between the axisymmetric and first azimuthal mode that has been reported in literature (Plaschko, 1979). Figure 6.7 shows that there is some variation between the phase velocity (ω/α) and the group velocity. If phase and group velocity were identical everywhere, the plot would be forced to be linear. The dispersive character of the wave is most apparent near the maximum growth rate.

In Section 1.4.3 of Chapter 1 it was observed how viscosity in some cases has a destabilizing effect, contrary to physical intuition. The results of Morris (1976) and Lessen and Singh (1973) are confirmed here in Figure 6.8 which shows the variation of the maximum growth rate with Reynolds number for a fully developed jet profile ($1/(1+r^2)^2$) and azimuthal mode number, m=1. Figure 6.8 shows how the growth rate first increases with Reynolds number then decreases and approaches an asymptotic growth rate at large Reynolds numbers. The shooting method with an outside Newton solver is very well suited for obtaining the maximal growth rate type of results shown in Figure 6.8.

The trailing line vortex profile (U(r) = e^{-x^2}, V(r) = q/r(1-e^{-x^2}) is shown in Figure 6.9. A more traditional result is recovered in the analysis of one of the inviscid

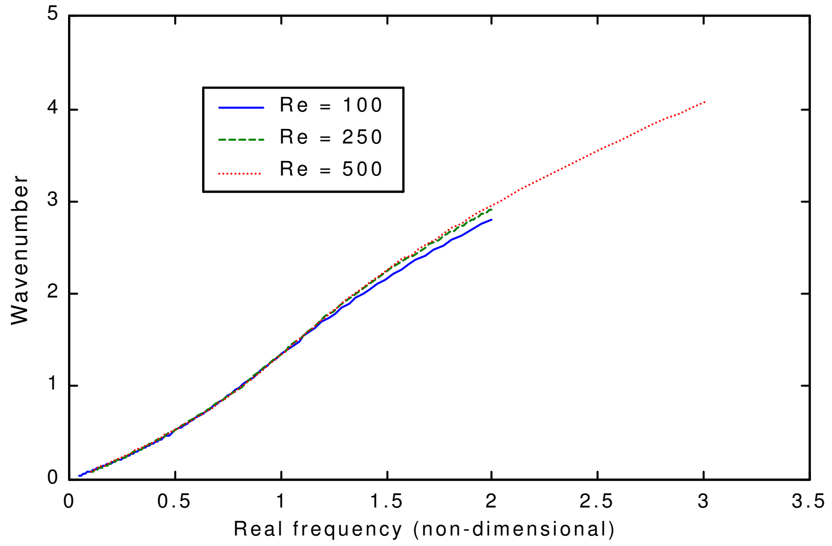

Figure 6.7: Plot of wavenumber as a function of real frequency for the tanh jet profile for three Reynolds numbers with m = 0

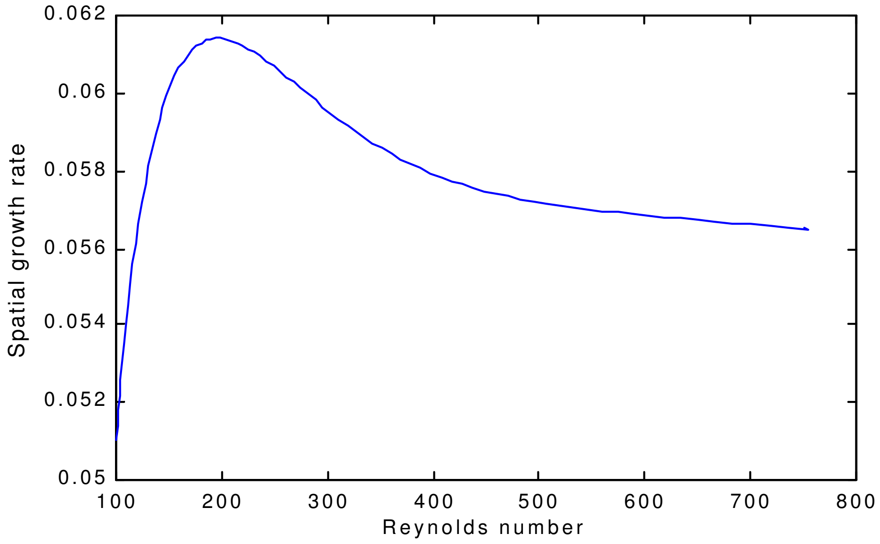

Figure 6.8: Plot of maximum growth rate as a function of Reynolds number for the fully developed jet profile

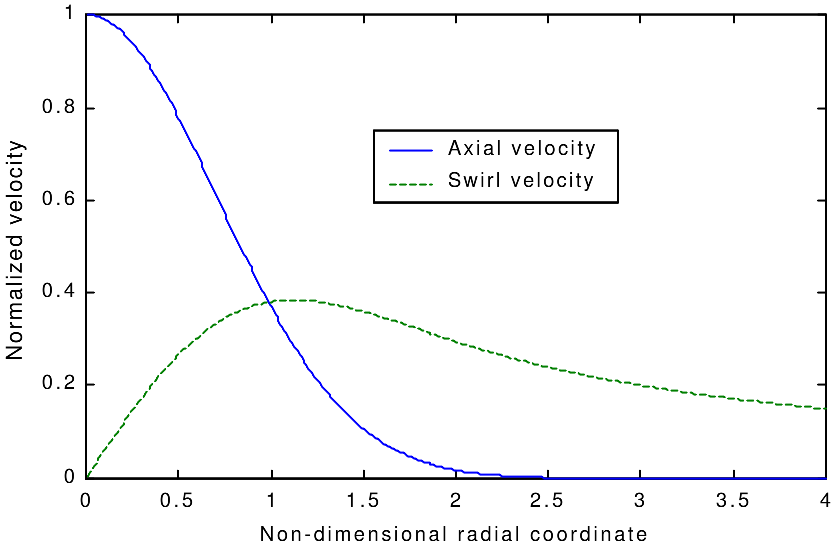

Figure 6.9: Trailing line vortex for q = 0.6

modes observed by Khorrami and Malik (1989). Figure 6.10 shows the variation of temporal growth rate near the maximum real axial wavenumber (α=1.34) with Reynolds number for the case of q=0.6 and the second negative azimuthal mode (m=-2). The results presented in Figure 6.10 are an example of temporal stability analysis where the wavenumber is kept real and the temporal frequency becomes the eigenvalue. As expected the growth rate asymptotically approaches a maximum as Reynolds number is increased.

Finally, the absolute stability results of the ring-jet with swirl, as studied by Michalke (1999) are presented briefly. The velocity profile will be examined in much more detail with respect to the experimental study reported here in Section 6.7. The velocity profile is given analytically in Equation 6.31. For the results presented, the profile shown in Figure 6.11 was used. The parameters for this profile are U_{oM}=-0.30 and $N_M = 1$. The Reynolds number for the results is equal to 1000 and the first azimuthal mode is studied. It should be noted that Michalke (1999) performed the absolute instability analysis on the inviscid disturbance equations whereas the results

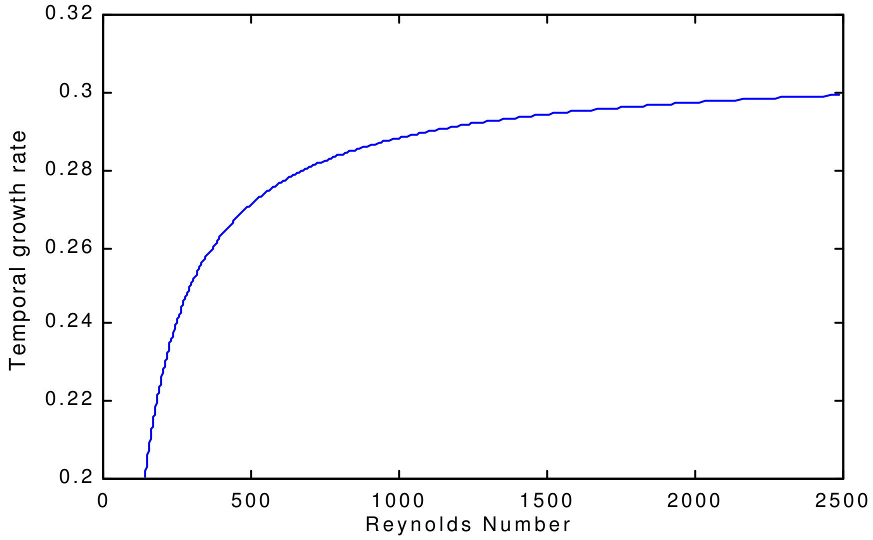

Figure 6.10: Plot of temporal growth rate as a function of Reynolds number at α = 1.34 and q=0.6, m=-2

presented here are based on viscous analysis. No study of axisymmetric viscous linear absolute stability with swirl has been published to date.

$$\begin{aligned} U(r) &= 4B_M C_M(r)[1 - B_M C_M(r)] \\ C_M(r) &= [1 + (e^{ar^2} - 1)^N_M]^{-1} \\ B_M &= 0.5[1 + \sqrt{(1 - U_{oM})}] \\ a_M(U_{oM}) &\text{ is given by: } \quad U(1) = 1 \\ W(r) &= \frac{A_M}{r}\left[\frac{1 - e^{-b_M r^2}}{1 - e^{-b_M}}\right] \\ b_M &= 1.2564315 \text{ for W(1)} = max(W(r)) = A_M \end{aligned} \tag{6.31}$$

Figure 6.12 shows the variation of the absolute growth rate of the first azimuthal mode with swirl strength for the ring jet shown in Figure 6.11. It is seen that the instability mode rotating with the flow becomes absolutely unstable and that the usually very convectively unstable negative azimuthal mode (analogous to negative A) is actually stable. Note also that very high swirl will stabilize the flow. No

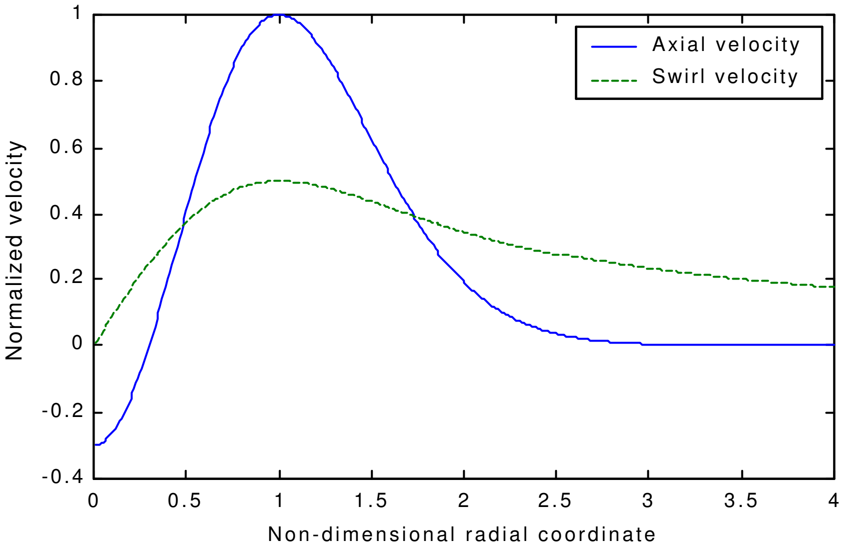

Figure 6.11: Ring jet profile analyzed in Figure 6.12

absolute instability was found for the axisymmetric azimuthal mode. In terms of computational effort, Figure 6.12 represents about ten hours of computational time, indicating that absolute viscous stability analysis is relatively taxing.

6.7 Linear stability of experimentally observed flows

The results of linear stability analysis of selected flow profiles will be reported. An exhaustive linear stability analysis (every local profile) could not be justified in light of the experimental results which show very little coherent motion. Some flows are however extremely dynamically interesting and the analysis will focus on these.

6.7.1 Obtaining flow profiles from experimental data

To perform linear stability analysis on the measured flow fields, a smooth analytical form of the profiles must be obtained for each flow field to be analyzed. Some additional requirements restrict the flexibility in the analytical form further. For ex-

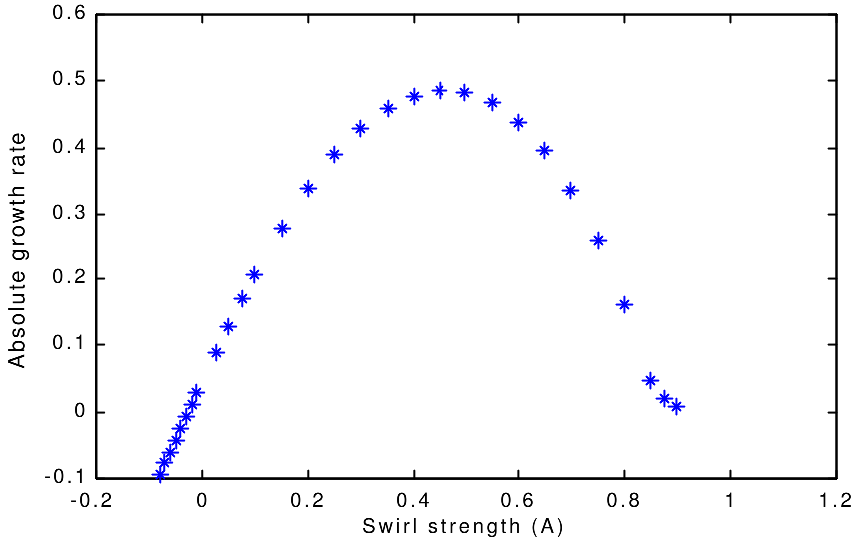

Figure 6.12: Variation of absolute growth rate with swirl strength for the ring-jet profile shown in Figure 6.11

ample, analytical forms could not contain fractional powers since these do not allow a far field asymptotic integer power series expansion to be formed. The requirement falls away if the resulting function decays rapidly enough to be assumed zero at the radius where asymptotic solutions are matched (e.g. ring jet). Additionally, to facilitate the fitting of some function types, the reference and normalizing length for linear stability analysis is the radius of the nozzle, not its diameter as before. The reference length is the same whether annulus or free vortex geometries are analyzed.

For the axial velocity profile, two main velocity profile types were used. The first is given in Equation 6.32, and consists of the superposition of a decaying exponential and a hyperbolic tangent profile. The equation allows the axial momentum surplus at the centerline of the free vortex geometry to be modeled as well as the axial momentum deficit in the wake type flows seen in the combustor. The profile is most suitable when a nearly flat velocity profile exists along part of the radius. The parameters in the profile allow for selective re-scaling of the radial coordinate for the hyperbolic tangent so that the shear layer can be placed accurately with respect to the experimental data.

$$u_{est}(r) = \frac{p1}{2} \left[1 + \tanh\left(p2\left(\frac{1}{r} - r\right)\right)\right] + p3e^{(-p4)(r^{p5})} - p6; \tag{6.32}$$

The second velocity profile is a parameterized version of Michalke's ring jet. The analytical form for the velocity profile is given in Equation 6.33. The profile allows for external back-flow which can be changed parametricaly without affecting the rest of the fit profile.

$$\begin{aligned} u_{est}(r) &= (p4\ (1 + p5))\ \ (4B_M C_M(r)[1 - B_M\ C_M(r)]) - p5 \\ C_M(r) &= [1 + (e^{p2\ r^2} - 1)^{p3}]^{-1} \\ B_M &= 0.5[1 + \sqrt{(1 - U_{oM})}] \\ U_{oM} &= \frac{(p1\ p4 + p5)}{(p4\ (1 + p5))} \end{aligned} \tag{6.33}$$

Only one generic type of velocity profile was able to capture most of the swirling flow velocity distributions encountered. The profile consists of a free vortex type profile (similar to trailing line vortex) with a superimposed hyperbolic tangent profile. The coefficients of the hyperbolic tangent profile are set to zero for semi-infinite domain calculations. The radial coordinate of the hyperbolic tangent profile has a re-scaling parameter to move the hyperbolic tangent swirl shear layer radially. The generic swirl velocity fit is given in Equation 6.34

$$w_{est}(r) = \frac{p1}{r^{p2}}\ \frac{\left[1 - e^{-p3\ (r^{p2+1})}\right]}{(1 - e^{-p3})} + p4\ \left[\tanh\left(p5\ (\frac{1}{(p7\ r)} - (p7\ r))\right) - 1\right] -\ p6\ r \tag{6.34}$$

6.7.2 Laminar stability analysis results

6.7.2.1 Plain jet velocity profile study

In both experimental configurations studied, the external shear layer of the flow exiting from the nozzle resembles that of the hyperbolic tangent jet as shown in earlier in Figure 6.3. As the flow evolves downstream, the external shear layer thickens.

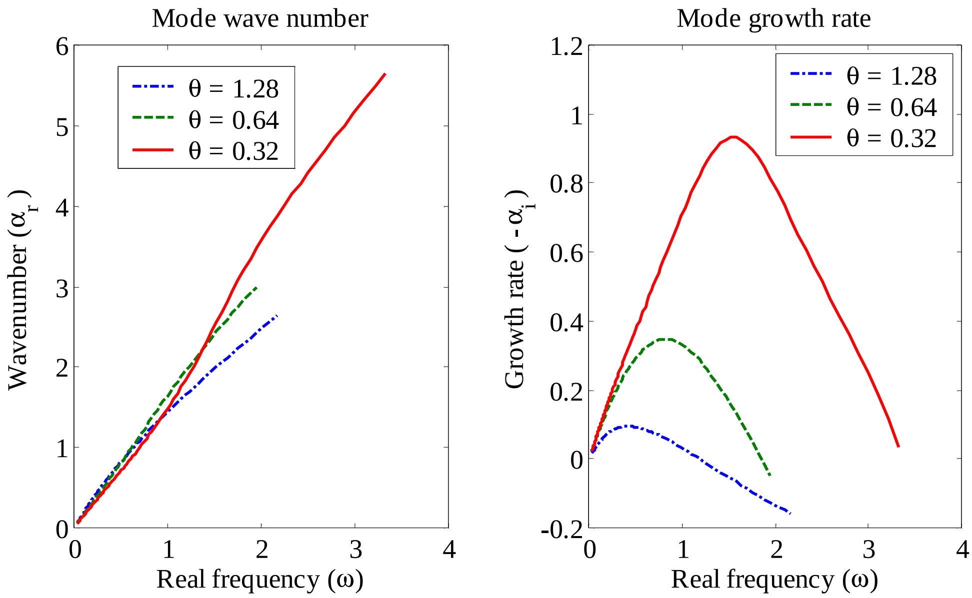

Figure 6.13: Hyperbolic tangent jet - stability characteristics as a function of shear layer thickness - m=1

Figures 6.13 and 6.14 show how the convective stability characteristics change as the shear layer thickness changes for the first azimuthal mode and the axisymmetric mode respectively. Note that because these profiles do not include the effect of swirl, the stability characteristics are not a function of the sign of the azimuthal mode number.

The figures show that as the shear layer thickens, significant stabilization occurs for both azimuthal modes but the axisymmetric mode is much more rapidly stabilized, even though initially for the thinnest shear layer studied, the growth rate for the axisymmetric mode is greater than that for the first azimuthal mode. The figures also clearly show a downward shift in the range of amplified frequencies as the shear layer thickens, and the flow develops downstream. Furthermore, the range of amplified frequencies becomes smaller as the shear layer thickens increasing the likelihood that spectral coloration of the turbulence will occur in the measured spectra of velocity.

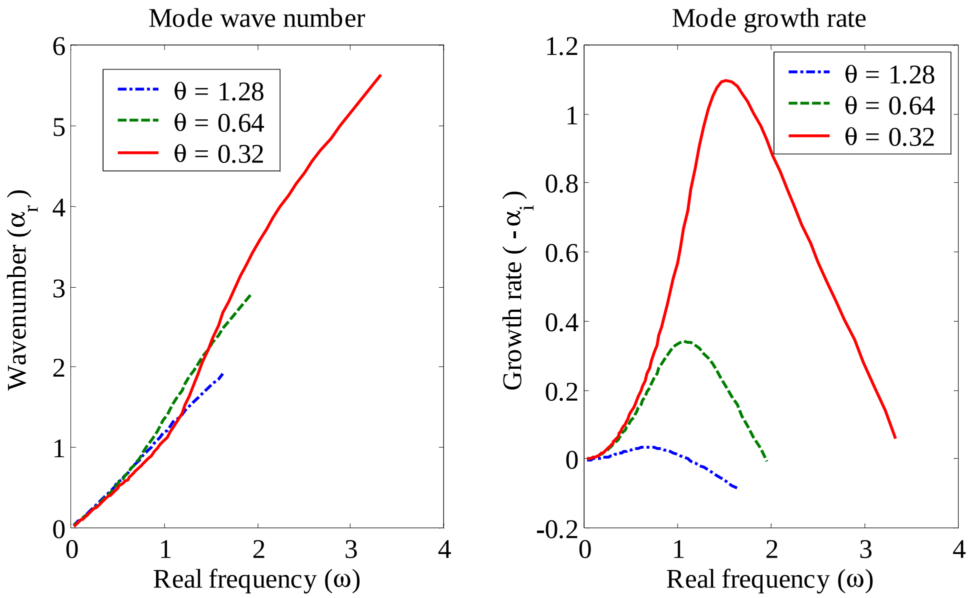

Figure 6.14: Hyperbolic tangent jet - stability characteristics as a function of shear layer thickness - m=0

6.7.2.2 Free vortex nozzle velocity profile for S=0.21

The first of the profiles analyzed using the laminar stability analysis is the flow encountered in the nozzle at S=0.21 for 50 SCFM. The analysis is performed using the analytical fit (Equation 6.32 and 6.34) to experimental data shown in Figure 6.15. The fit captures the axial momentum surplus at the centerline and uses a half hyperbolic tangent profile to model the outside boundary layer. The calculations were performed using a Reynolds number of 1000 to be near the inviscid limit.

Figure 6.16 shows the results for the least stable mode found in spatial stability analysis. No unstable modes were found, although the mode presented here likely will achieve positive growth rates in the inviscid limit. The least stable mode was found with azimuthal wave number (m) equal to -1.

The least stable mode is not associated with the wall shear layer. Figure 6.17 shows the disturbance eigenfunctions corresponding to point of lowest damping in the real frequency range, ω=1.7. Note again that this is a non-dimensional circular frequency Strouhal number. The equivalent cyclic frequency Strouhal number based

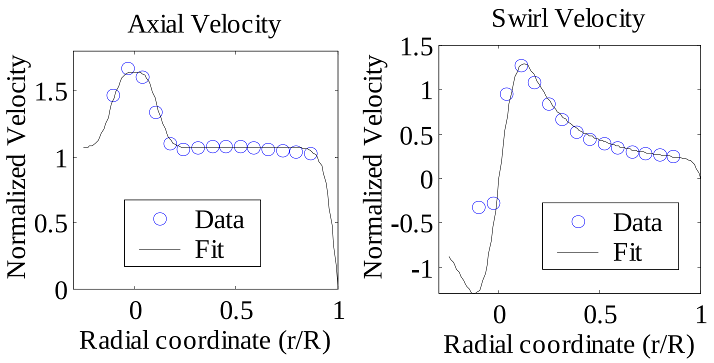

Figure 6.15: Analytical profile fit and experimental data for nozzle S=0.21 profile

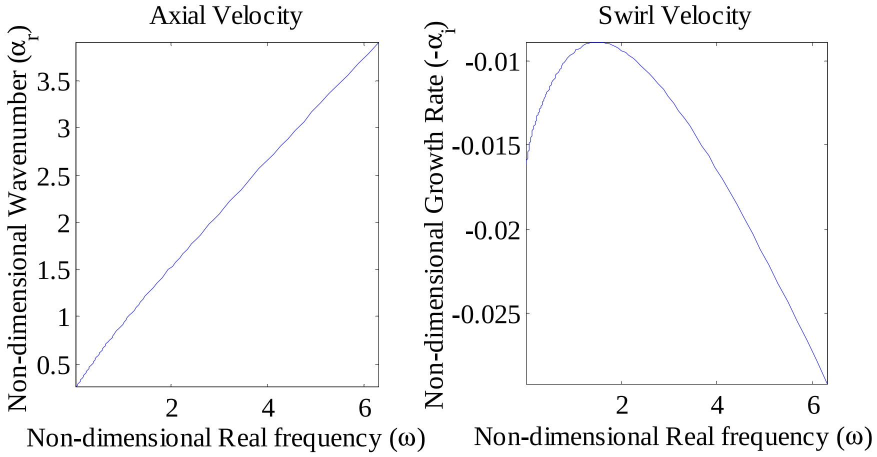

Figure 6.16: Least stable mode for nozzle S=0.21 flow profile

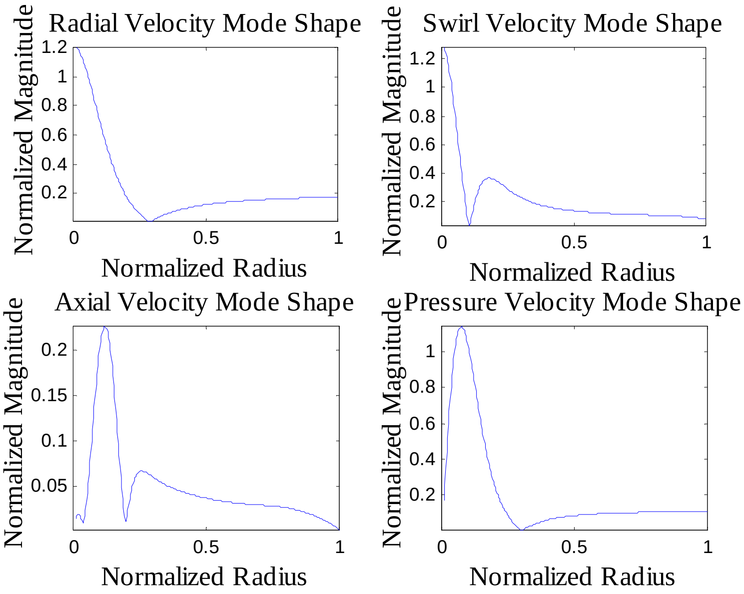

Figure 6.17: Eigenfunctions at least stable point for nozzle velocity profile

on the experimentally used reference length is St=0.54. The eigenfunctions clearly show that the least stable mode is associated with the vortex core, indicating that the presence of the axial momentum surplus and swirl do have an influence on the stability properties of the flow field, even when the flow is confined inside the nozzle.

6.7.2.3 Free vortex combustor velocity profile for S=0.21

Figure 6.18 shows the analytical profile fit (Equation 6.32 and 6.34) for S=0.21 and Q=50 SCFM also but in the combustor at x=0.44 (non-dimensionalized with diameter). The profile has two shear layers, the outer shear layer associated with jet flow from the nozzle into the sudden expansion and the inner shear layer associated with the swirl induced wake at center of the flow. The fit used here does not capture the swirl velocity increase beyond the outer shear layer.

The profile was once again analyzed for spatial stability over a range of real frequencies. The first negative and positive azimuthal modes, as well as the axisymmetric modes were calculated. Figure 6.19 shows the results for the three most unstable modes for each of the calculated azimuthal wavenumbers. The results are very similar

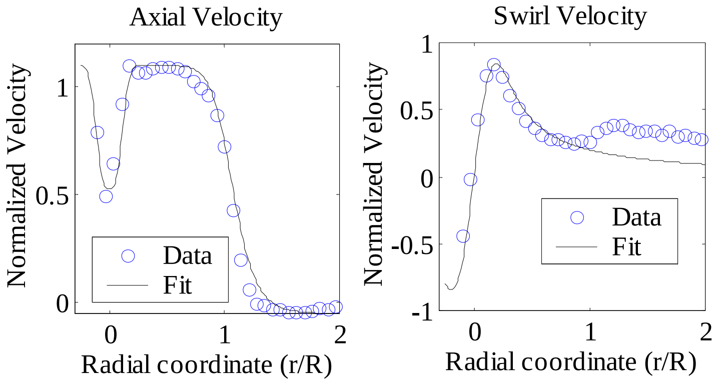

Figure 6.18: Analytical profile fit and experimental data in the combustor for S=0.21 at x/D_n=0.44

to those seen for the hyperbolic tangent profile with $\theta = 0.32$ in Figure 6.13 and 6.14. The notable difference is that the positive azimuthal mode is relatively stabilized by the swirl, whereas the negative azimuthal mode maintains high growth rates. All three azimuthal wavenumber modes however exhibit large growth rates over a wide range of frequencies, and with a swiftly developing flow, it is unlikely that spectral energy concentrations can be distinguished in the velocity spectra. The instability characteristics thus appear to be dominated by the outer shear layer dynamics. Influence of the inner shear layer due to the wake cannot be identified in the most unstable mode dynamics.

Note that the fit to the experimental data did not incorporate the increase of swirl beyond the outer shear layer. The change in the distribution of the shear, which is mostly responsible for the dynamics, would not change significantly however because the shear introduced by the increase in swirl is very low.

To investigate the stability characteristics of the wake profile further, the swirl was neglected and the stability characteristics calculated. The results of the analysis are summarized in Figure 6.20. For the zero swirl case, an unstable inner shear layer mode can be identified. The peak amplification occurs at Strouhal numbers far above those seen for the outer shear layer. The increase in frequency corresponds to the smaller scale of the inner wake. The dominant physical scale for this mode is the

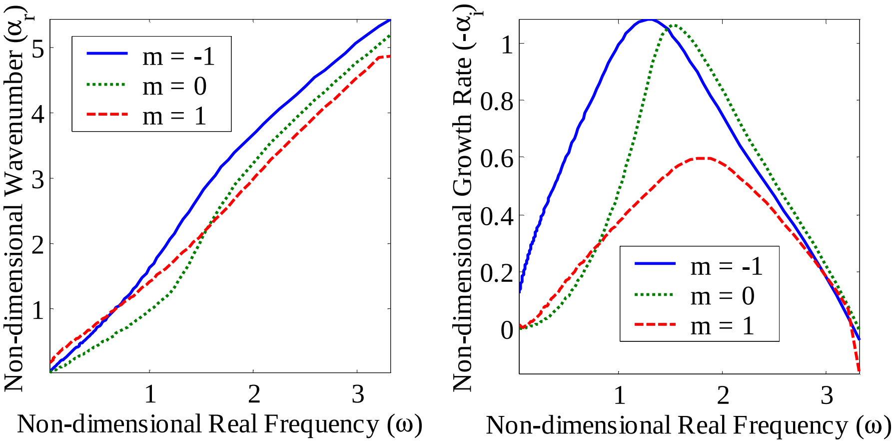

Figure 6.19: Comparison of azimuthal wavenumber stability characteristics in combustor for S=0.21

width of the wake, and not the diameter of the nozzle as it is for the outer shear layer. The width of the wake is several times smaller than the diameter of the nozzle.

Figure 6.20 also underlines the effect of swirl, as the axisymmetric mode is now the most unstable mode for the profile studied. The overall growth rates and locations

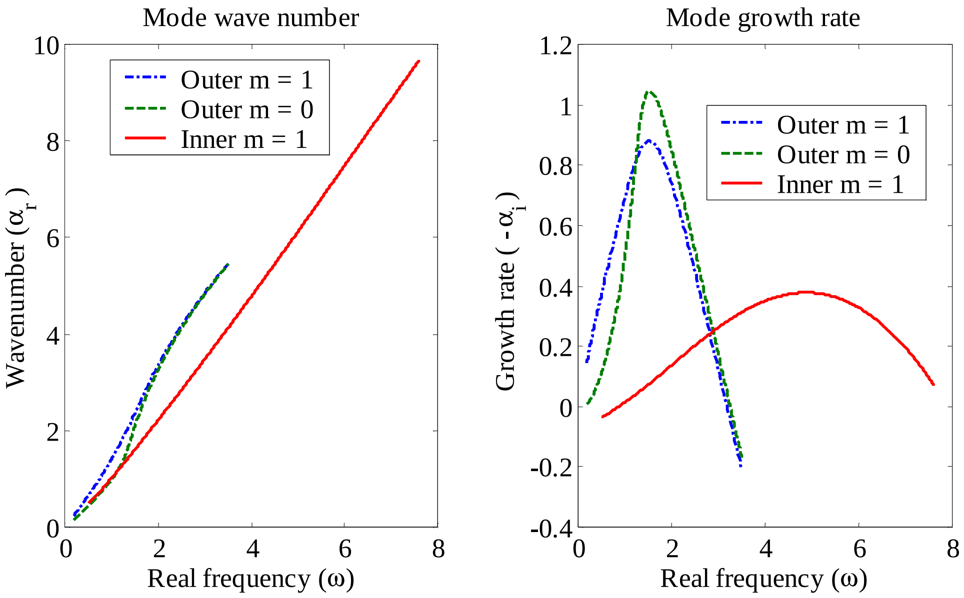

Figure 6.20: Stability characteristics of S=0.21 axial flow profile w/o swirl

of maximum growth rate are relatively unchanged from the characteristics calculated with swirl, again supporting the claim that the addition of swirl has only a secondary influence on the outer shear layer stability characteristics. The same is not true for the outer shear layer. Figure 6.21 shows how the wavenumber and growth rate vary at constant St=6 as the fraction of total swirl is varied. Negative swirl fractions mean that the swirl direction is reversed from that in the experiments. Since the variation is for the m=1 mode, negative swirl fractions will calculate the m=-1 stability characteristics of the corresponding positive swirl fraction. Figure 6.21 shows that as swirl is increased from zero, the wake is initially drastically destabilized for the positive azimuthal wavenumber. The negative azimuthal wavenumber mode is in contrast immediately stabilized and remains stable. Further increases in the amount of swirl also eventually stabilize the positive azimuthal wavenumber mode and even only at 50% of the actual experimentally observed swirl the damping in the inner shear layer mode is very high. The variation of growth rate with frequency of these modes was investigated for a swirl fraction of 0.5 but no positive growth rates are found although there is a shift of the minimum damping point to lower frequencies with the addition of swirl.

The rapid stabilization of the wake mode for negative azimuthal wavenumbers as swirl is increased is a very significant finding and will help explain the absolute instability characteristics discussed hereafter.

6.7.2.4 Annulus combustor velocity profile for S=0.60

Figure 6.22 shows the results of an analytical fit (Equation 6.33 and 6.34) to the annulus geometry velocity profile at the first measured station in the combustor (x=0.63 - non-dimensionalized by hydraulic diameter of annulus geometry). The fit captures the inner parts of the flow field very well. In the outer part of the flow field, the analytical model fails to capture the recirculation zone in the axial velocity profile and the much slower decay in the swirl velocity.

The parameterized ring jet profile is similar to that studied by Michalke (1999) and based on the experimental results presented is expected to be absolutely unsta-

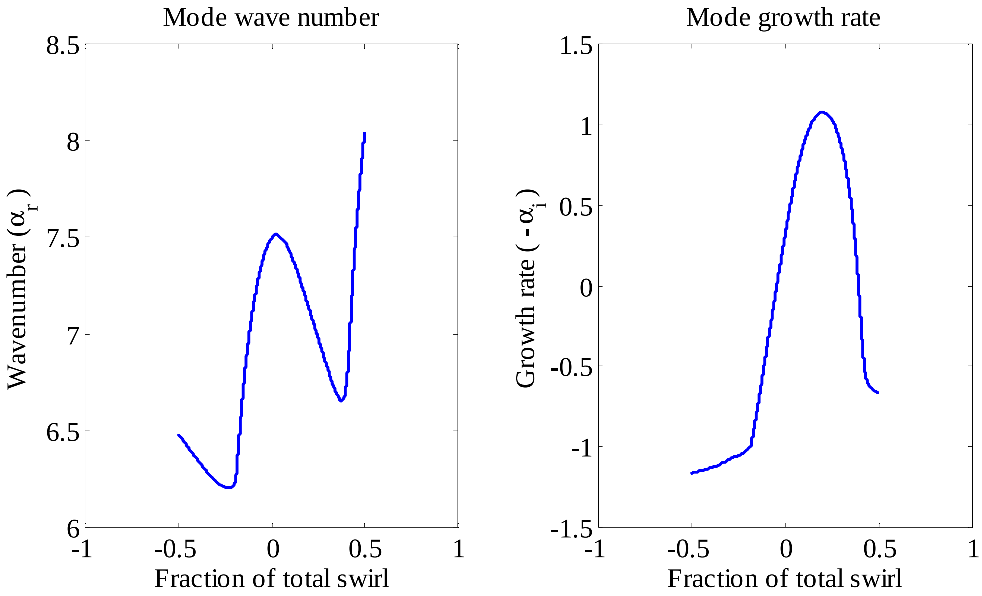

Figure 6.21: Wake mode stability as a function of swirl fraction

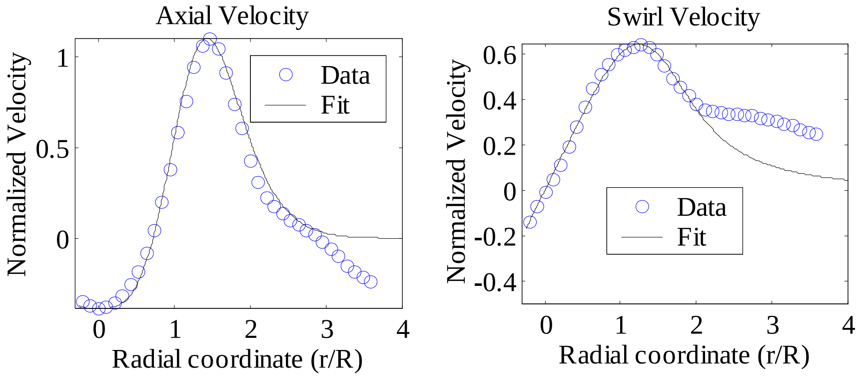

Figure 6.22: Analytical profile fit and experimental data in the combustor for S=0.60 at x/D_n=0.44

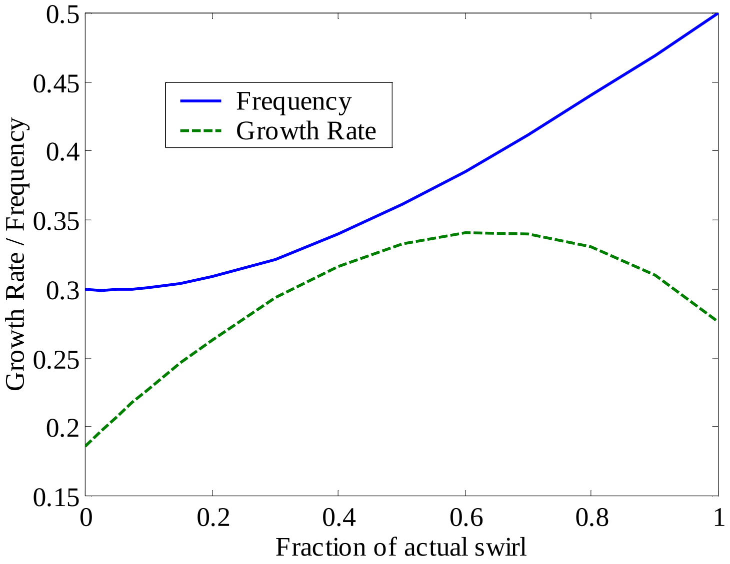

Figure 6.23: Absolute frequency and growth rate for annulus geometry as a function of swirl strength

ble. Figure 6.23 shows the results of the absolute stability analysis for a varying fraction of the actual swirl in the experimental profile. The flow is indeed found to be absolutely unstable with azimuthal wavenumber 1. The maximum absolute growth rate is achieved at 60% of the actual swirl profile. The curves shown in Figure 6.23 qualitatively resemble those found by Michalke (1999). The non-dimensional cyclic frequency Strouhal number equivalent to the circular frequency Strouhal number based on radius reported here is 0.18. The absolute frequency calculated by the absolute stability analysis is thus about half that observed in the experiments.

Figure 6.24 shows the eigenfunctions calculated at the point of absolute stability. Some similarities with experiments can be distinguished here. The axial velocity eigenfunction has by far the highest magnitude of energy. The axial eigenfunction exhibits three interior eigenfunction nodes and as required by the boundary conditions, the axial eigenfunction is zero at the centerline. Some of the key differences include that experiments showed most energy was contained in the first relative maximum, not the second. The swirl eigenfunction does not have a relative maximum at the flow center, as was observed in the experiments.

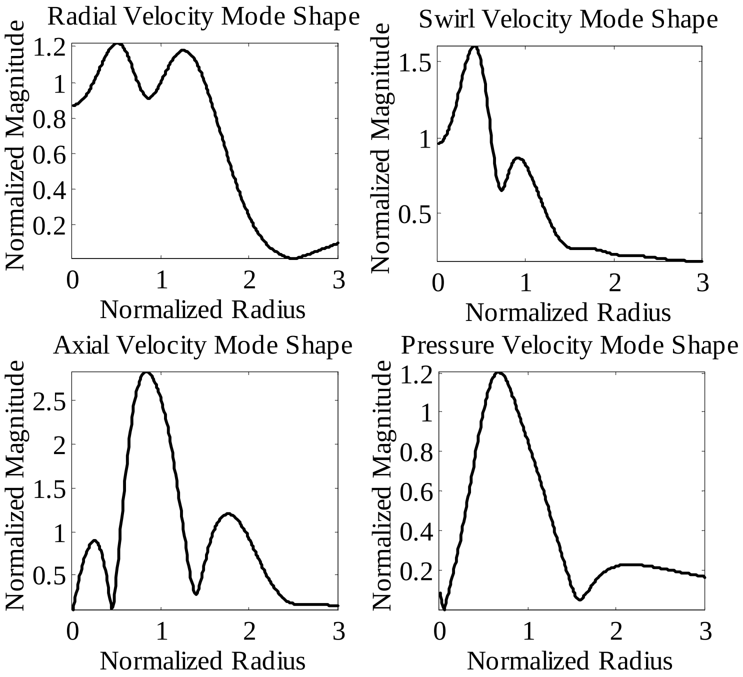

Figure 6.24: Eigenfunctions for full swirl saddle point

However, some of the differences in swirl eigenfunction are due to experimental limitations in the measurement of swirl velocity fluctuations at the center of the flow field. The fact that the experimental results show a maximum of oscillation strength at the center of the flow field can be attributed to the fact that the component measured here is not truly the swirl component of velocity. At the exact center of the flow, the component measured is purely radial and with some small misalignment, the immediate neighborhood of the center will also contain some radial velocity fluctuation information. There are no contributions to the mean velocity due to this error because the radial velocity must go to zero at the center of the flow field for an axisymmetric mean flow.

To attempt to match experimental results more accurately external back-flow was gradually added to the flow profile. However, no significant change in the dynamics was found, even for back-flow of 20%.

The lack of accuracy in the prediction of the instability frequency is perhaps disappointing but together with the wake stability characteristics discussed above a more thorough understanding of the absolute instability origin can be formed. Above, it was noted that swirl destabilizes the negative azimuthal mode of the external shear layer. Since the instability characteristics appear to be dominated by outer shear layer dynamics it would be natural to expect absolute instability to occur for negative azimuthal wavenumbers. However, the experiments and the analysis described here find that the absolute instability has azimuthal wavenumber of positive 1. The condition for absolute instability was described above as the coalescence to a saddle point of two modes, an upstream and a downstream mode. The question answered here is where do these two modes originate.

The absolute instability observed can be explained as a resonance between the inner and outer shear layer of the flow field. The azimuthal wavenumber of the resonance is positive one because the inner shear layer is stabilized with swirl for m=-1. Although the growth rates for the outer shear layer positive azimuthal wavenumber mode are lower, they are still positive. Only for the m=1 mode is it possible to have both an unstable inner and outer shear layer mode and thus the required resonance for absolute instability. The eigenfunctions calculated for the saddle point clearly show the interaction of the inner and outer shear layer, as the eigenfunction shows traces of both.

Absolute instability disappears in the experiments below S=0.35, as the center recirculation weakens. Simultaneously, the radially outward deflection of the entering annular jet significantly decreases, causing the wake at the center of the flow field to become not only weaker but also narrower. In view of the wake stability characteristics the absence of the absolute instability can be explained as the result of a lack of overlap in the scales of instability of the inner and outer shear layer. As the wake becomes narrower, the range of amplified frequencies for the wake shifts upward and away from the range of amplified frequencies of the outer shear layer. Intuitively, overlap in amplified frequencies alone is not enough to allow resonance, the eigenfunctions must show commensurate scales also.

The explanation of absolute instability thus put forth does not rely on the existence of reverse flow although reverse flow may be required to form the necessary "upstream" mode. More importantly, the instability is described as a superposition onto the flow field having very little influence on the behavior of the mean flow field itself. In other words, the description of the evolution of the mean flow field under changes in swirl does not require accounting for the influence of the absolute instability on the mean flow. Clearly there is an effect of such a large coherent oscillation on the mean flow field but the primary characteristics are still best described as in Chapter 4 using a balance between radial pressure distribution effects and turbulence production effects (See Chapter 7).

6.7.3 Turbulent stability analysis

Figure 6.25 shows a comparison between the model of kinetic energy distribution and experimental data for a flow rate of 50 SCFM. The estimate of turbulent kinetic energy is obtained by summing the squares of the RMS velocities. The radial RMS velocity is estimated as half the square root of the sum of the axial and swirl RMS velocities. Assuming a length scale of 0.01 m (about equal to the vortex core diam-

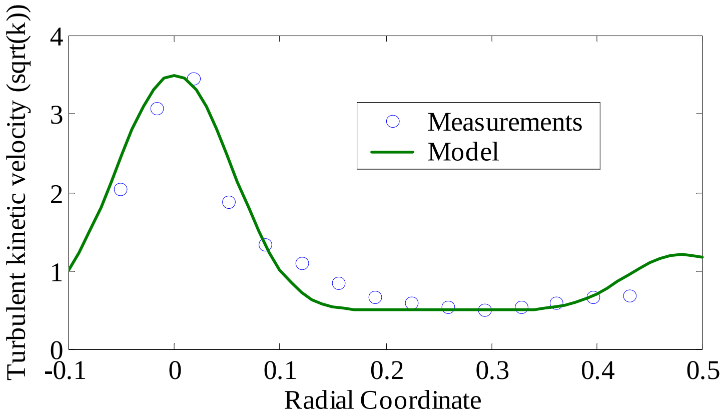

Figure 6.25: Modeled and actual turbulent kinetic velocity distribution for S=0.21, Q=50 SCFM

eter), the highest effective Reynolds number in the flow is approximately 175 (based on diameter). Accounting for turbulence thus introduces significant viscous effects even disregarding the non-uniform distribution. Note that laminar viscosity effects are dwarfed in comparison to turbulence effects.

To study the influence of turbulence, the analysis is applied to the nozzle profile studied above under constant viscosity. As shown in Figure 6.26, the addition of non-uniform viscosity in the flow field causes a frequency dependent stabilization and destabilization of the flow to occur. The figure shows the stability of the flow for the Reynolds number of the background turbulence, the minimum level of turbulence. The non-uniform component is then added in increments of 25%. Even at 25% of the complete model non-uniform turbulence, a significant stabilization of high frequencies occurs. The effects of stabilization decrease with decreasing frequency. Relative to the 25% non-uniform turbulent case, higher non-uniformity causes destabilization of the flow field but overall, at none of the frequencies in the studied range is the destabilization great enough to make the flow unstable or result in a lower amount of damping than that calculated for the background amount of turbulence.

The effects of viscosity here thus in large part help to stabilize the flow, even if the stabilization is not even for all frequencies of disturbance. Non-uniform turbulence thus does not explain the loss of stability of the vortex in the nozzle flow. However,

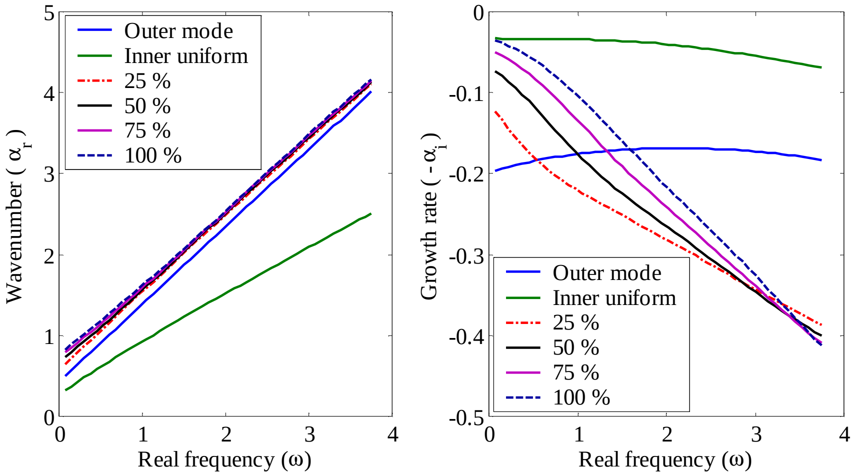

Figure 6.26: Results of turbulent stability analysis for nozzle S=0.21 profile (m=-1)

the mechanism discussed in Chapter 4 for the loss of stability in the nozzle remains viable. The simple turbulence model used here can only account for the viscous effects of turbulence. The model cannot account for vortex movement or the large amount of low frequency energy contained in the turbulence fluctuations.

Turbulent linear stability analysis thus was found not able to capture or predict the important vigorous turbulent motion found in the free vortex geometry nozzle flows. The loss of stability in vortex core is described in Chapter 4 as a complicated process involving the concept of kinetic energy saturation of the vortex core. Such a concept cannot be captured by linear stability analysis and the failure of linear stability can only be seen as underlining the global characteristics of the loss of stability of the vortex core in free vortex geometry flows. Further discussion on this topic will follow in Chapter 7.